



Inferring processes governing cloud transition during mid-latitude marine cold-air outbreaks from satellite

Jianhao Zhang^{1,2}, David Painemal³, Tom Dror^{1,2}, Jung-Sub Lim^{1,2}, Armin Sorooshian^{4,5}, and Graham Feingold²

Correspondence: Jianhao Zhang (jianhao.zhang@noaa.gov)

Abstract. Cloud morphological transitions strongly influence radiative effects and the regional radiation budget. Marine coldair outbreaks (MCAOs) over the northwestern Atlantic feature such transitions, from overcast stratiform to broken cumuliform cloud fields downwind. Characterizing these transitions requires an understanding of the thermodynamic and dynamical evolution of the marine boundary layer and the interplay between warm- and cold-phase processes. Using a novel 'space-time exchange' approach, we construct instantaneous trajectories using reanalysis winds and extract geophysical variable traces along these trajectories from GOES-16 satellite snapshots for five MCAO events sampled during the NASA ACTIVATE campaign (2020–2022). Clear directionality of traces in liquid water path (LWP)-droplet number ($N_{\rm d}$) space reveals sequential dominance of drop activation, condensational growth, and collision-coalescence during cloud thickening. Patterns of traces in domain-LWP versus domain-IWP (ice water path) suggest fingerprints of two distinct mixed-phase processes: (i) gradual liquid depletion via vapor deposition and (ii) rapid depletion via riming, preceded by co-growth of liquid and ice. Elevated $N_{\rm d}$ suppresses peak LWP and delays cloud breakup. A large spread in shortwave albedo is found during cloud transition, reflecting mixed-phase processes. Metrics denoting cloud organization converge towards the end of the transition, despite differences in cloud micro- and macro-physical properties among cases. These results underscore the central role of frozen hydrometeors in governing cloud transitions and demonstrate a powerful framework for process inference based on satellite snapshots using the 'space-time exchange' approach. This framework offers a new pathway to benchmarking model representations of mixed-phase microphysics and advancing model-observation synergy.

1 Introduction

About one-third of the sunlight-absorbing ocean surface is covered by marine boundary layer clouds (Klein and Hartmann, 1993). Their close proximity to the sea surface and high reflectivity of sunlight result in a net cooling effect on the Earth's energy budget (Forster et al., 2021). The radiative properties of these clouds are governed collectively by the available water surface of cloud droplets at the microscopic scale and the amount and areal extent of the water condensate at the macrophysical

¹Cooperative Institute for Research in Environmental Sciences (CIRES), University of Colorado, Boulder, CO, USA

²Chemical Sciences Laboratory, National Oceanic and Atmospheric Administration (NOAA), Boulder, CO, USA

³NASA Langley Research Center, Hampton, VA, USA

⁴Department of Chemical and Environmental Engineering, University of Arizona, Tucson, AZ, USA

⁵Department of Hydrology and Atmospheric Sciences, University of Arizona, Tucson, AZ, USA





scale (Twomey, 1974; Wood, 2012). As the ocean surface continues to warm in response to increasing greenhouse gas (GHG) emissions, these clouds can act as either a buffer or an amplifier to the warming, depending on how they adjust to the changing boundary layer conditions. Therefore, understanding the processes that govern boundary layer clouds and representing them in large-scale models becomes critical to predicting future warming rates. To date, Earth system models continue to struggle on this front, in part due to the insufficient grid spacing needed to resolve these clouds and the simplified representation of the intricate interactions between clouds and their environment (Zelinka et al., 2020; Bellouin et al., 2020).

Morphological boundary layer cloud transitions, particularly those from overcast to broken cloud fields with profound radiative impacts (McCoy et al., 2017; Goren et al., 2022), are extensively studied to understand and characterize the processes governing the cloud evolution. A common type is the stratocumulus-to-cumulus or closed-to-open cell transition. These transitions typically occur within a deepening marine boundary layer driven by a gradient in the sea surface temperature (SST) aligning with the prevailing wind, such as the one moving from subtropical ocean upwelling regions to warm, tropical waters (Albrecht et al., 1995; Bretherton, 1992; Sandu et al., 2010) and the one moving off the ice or the continental edges during marine cold-air outbreaks (MCAO; Brümmer, 1996, 1999; Fletcher et al., 2016a, b; Pithan et al., 2018). Inherently, cloud transition is a multi-scale problem. As the marine boundary layer (MBL) is advected over a warmer ocean surface, strengthening surface fluxes deepen the MBL, entraining free-tropospheric air and eventually causing the cloud layer to be decoupled from the surface source of moisture and break-up (Bretherton and Wyant, 1997; Wyant et al., 1997; Sandu and Stevens, 2011). Concurrently, the onset of warm rain and drizzle, through the build up of cloud water and the collision-coalescence process, facilitates the transition from a stratiform to a more convective MBL regime and accelerates cloud break-up via aerosol scavenging (Stevens et al., 1998; Abel et al., 2017; Yamaguchi et al., 2017; Goren et al., 2019). Moreover, when conditions are met for mixed-phase clouds, processes involving frozen hydrometeors such as riming and secondary ice processes can further ramp up the removal of cloud water and the closed-to-open cloud transition during an MCAO (Abel et al., 2017; Tornow et al., 2021; Karalis et al., 2022; Chellappan et al., 2024). Accurately capturing the onset of the transition remains a challenge even for process-resolving models due to the sensitivity of transition onset to the representation of microphysical processes in the models (e.g., Abel et al., 2017; de Roode et al., 2019).

Polar-orbiting satellites offer detailed observations of boundary layer clouds at (sub-)kilometer resolution (e.g., Platnick et al., 2003), but the lack of temporal coverage prevents the tracking of the spatiotemporally evolving cloud system to study the time-dependent processes governing cloud evolution. Geostationary satellites offer such capability and have been used to study subtropical stratocumulus-to-cumulus transitions (e.g., Christensen et al., 2020), but the reliance of their cloud microphysical retrievals, e.g., cloud droplet number concentration (N_d), on shortwave channels limits the temporal coverage to sunlit hours. Given the timescale at which cloud transitions occur, $\mathcal{O}(\sim \text{day})$, a complete characterization of the transition proves to be challenging.

In this study, we apply a 'space-time exchange' to geostationary satellite snapshots to construct "instantaneous" trajectories that approximate Lagrangian cloud transitions, enabling us to capture the complete closed-to-open cloud transition during MCAO events. Derived from the original concept of ergodicity (Boltzmann, 1884)—the mean state of the system can be characterized by either a collection of individual realizations of the system or, equivalently, by tracking one realization over



65



time—this 'space-time exchange' approach has been applied in the field of atmospheric science, particularly in studies aiming at cloud process characterization (e.g., Feingold et al., 2025; Goren et al., 2022; Murray-Watson et al., 2023).

Cloud systems are complex, multi-scale, dynamic by nature, and are slaved to the large-scale meteorological conditions. The large number of degrees of freedom and intertwined processes makes process-inference from snapshot observation particularly difficult. On this front, recent studies have made promising advances in inferring cloud microphysical processes from snapshots of cloud systems using carefully selected combinations of geophysical variables (GVs), such as cloud fraction - albedo, liquid water path (LWP) - N_d , and optical depth - radar reflectivity (e.g., Suzuki et al., 2010; Feingold et al., 2016; Glassmeier et al., 2019; Hoffmann et al., 2020; Zhang et al., 2022; Zhang and Feingold, 2023; Feingold et al., 2025).

Here we use satellite-retrieved in-cloud LWP- N_d and areal-mean LWP-IWP (ice water path) relationships to articulate the manifestation of cloud microphysical processes in the context of deepening marine boundary layers as part of MCAO events occurring over the northwestern Atlantic Ocean during boreal winter. Instead of building statistics from a large sample of satellite snapshots, we illustrate the capability of this process-inference approach with selected MCAO case studies, supported by airborne in-situ measurements and remote sensing retrievals collected during the multi-year NASA Earth Venture Suborbital (EVS) campaign ACTIVATE (Aerosol Cloud meTeorology Interactions oVer the western ATlantic Experiment; Sorooshian et al., 2019, 2025). We find a key role of riming in driving the closed-to-open cloud transitions observed during ACTIVATE, consistent with recent findings in Tornow et al. (2021) and Chellappan et al. (2024). The 'space-time exchange' approach along with its underlying assumptions and datasets is introduced in Section 2. Results are shown in Section 3, followed by discussions (Section 4) and conclusions (Section 5).

75 2 Data & methods

2.1 Geophysical variables from GOES-16 snapshots

The Advanced Baseline Imager (ABI) aboard the 16^{th} Geostationary Operational Environment Satellite (GOES-16) is used to retrieve cloud properties based on the NASA Satellite ClOud and Radiation Property System (SatCORPS) algorithms, which primarily rely on the 0.65, 3.9, and 11.2 μ m channels for derivation of cloud microphysical properties (Minnis et al., 2008, 2021; Painemal et al., 2021). This study uses the SatCORPS produced cloud retrievals over a domain (29–46°N, 78–60°W) covering the ACTIVATE deployment region (Sorooshian et al., 2023). Cloud variables, including cloud mask and phase, temperature, height, and pressure, particle effective radius (ice and liquid), water path (ice and liquid), optical depth, and broadband shortwave albedo, are produced at the native resolution of the infrared channels, which is 2 km at nadir. N_d is calculated using the (sub)adiabatic assumption (Szczodrak et al., 2001; Quaas et al., 2006) as

85
$$N_{\rm d} = \frac{\sqrt{5}}{2\pi k} \left(\frac{f_{\rm ad} c_{\rm w}(T, P) \tau_{\rm c}}{Q_{\rm ext} \rho_{\rm w} r_{\rm e}^5} \right)^{1/2}$$
 (1)

where τ_c is the cloud optical depth and r_e is the cloud (water) droplet effective radius. A value of 0.8 is assumed for k, the width of the modified gamma droplet distribution (Martin et al., 1994; Painemal and Zuidema, 2011). The temperature-pressure-dependent condensation rate (c_w) is calculated based on GOES-16 retrieved cloud temperature (T) and pressure (P)



95

100



(Grosvenor and Wood, 2014). The adiabatic fraction (f_{ad}) is assumed to be 0.8 (typical for stratiform clouds) (Grosvenor et al., 2018). An extinction efficiency (Q_{ext}) of 2 (Bennartz, 2007) and a liquid water density (ρ_w) of 997 kg m⁻³ are used in the calculations. In order to minimize retrieval biases, additional filtering of $r_e > 2 \mu m$, $\tau_c > 1$, cloud phase identified as either 'water' or 'suspected water', and solar zenith angle (SZA) < 65° is applied (Grosvenor et al., 2018). We note that, to capture the optically thin roll clouds at the western edge of the deck during cloud emergence, relatively liberal thresholds for r_e and τ_c are applied.

2.2 Meteorological reanalysis from ERA5

Meteorological reanalysis fields, including SST, temperature and humidity profiles, surface latent and sensible heat fluxes (LHF and SHF), horizontal winds at 1000 hPa, and vertical velocity at 500 hPa, are obtained hourly at 0.25° from the European Centre for Medium-Range Weather Forecasts (ECMWF) fifth-generation atmospheric reanalysis (ERA5; Hersbach et al., 2020). The marine cold-air outbreak index (M-index; Kolstad and Bracegirdle, 2008), a measure of the strength of the MCAO event and the stability of the marine boundary layer, is calculated as the difference between the potential temperature at 800 hPa and the sea surface temperature (Fletcher et al., 2016a). Buoyancy fluxes (Q_B) are calculated following Chellappan et al. (2024) as

$$Q_{\rm B} = {\rm SHF} \times (1 + 0.6q_{\rm 2m}) + 0.6{\rm LHF}(\frac{c_{\rm p}}{L_{\rm v}})T_{\rm 2m} \tag{2}$$

where q_{2m} and T_{2m} are the specific humidity and temperature at a height of 2 m, and values of 1004 J kg⁻¹ K⁻¹ and 2.5·10⁶ J kg⁻¹ are used for the specific heat of air at constant pressure (c_p) and latent heat of vaporization (L_v) , respectively, in the calculations.

2.3 2DS images from ACTIVATE field campaign

ACTIVATE featured two spatially coordinated aircraft, a low-flying HU-25 Falcon and high-flying King Air, that conducted 162 joint flights across multiple seasons in each year between 2020 and 2022. Images of ice habits captured by a SPEC Inc. 2-dimensional stereo (2D-S: covering hydrometeors with diameter size spanning 29-1465 µm) imager onboard the low-flying Falcon aircraft are used to help interpret the composition of frozen hydrometeors in mixed-phase clouds during MCAOs (Kirschler et al., 2023). A deeper discussion of the ACTIVATE campaign's flight and instrument details is provided in Sorooshian et al. (2023).

2.4 Instantaneous trajectories—a 'space-time exchange'

A key focus of this work is to characterize the driving processes for the morphological transition from closed-cellular, overcast to open-cellular, broken cloud fields during mid-latitude MCAO events. Therefore, it is crucial for us to capture the complete cloud transition considering the limitation that satellite microphysical properties are only derived during daytime due to the algorithm reliance on visible and near-infrared channels. However, given a typical boundary layer wind speed of 15 m s⁻¹ during a mid-latitude MCAO event (Chellappan et al., 2024), Lagrangian trajectories typically travel less than 500 km in fetch during sunlit hours, which covers the cloud street and closed-cell stages well, but often falls short for the open-cell stage. For



125

130



example, on 24 January 2021, the fetch of the Lagrangian trajectories (solid red lines), initialized in the morning from the western edge of the cloud street, reaches the open-cell stage during the night (Fig. 1b). Therefore, a real Lagrangian approach would limit our capability in characterizing the full transition due to the reliance of cloud microphysical retrievals on shortwave channels.

A unique feature of MCAO is the persistence of the boundary layer wind field during the event, evident in the overlapping of time-evolving wind vectors in Figure 1a. Taking advantage of this feature, we examine the idea of representing cloud transition by sampling cloud variables from a single GOES-16 snapshot along forward trajectories advected by the wind field present at that time. Here, two types of forward, isobaric trajectories were generated for comparison using 1000 hPa winds for advection, following Gryspeerdt et al. (2019b) and Murray-Watson et al. (2023) for their success in tracking the movement of low-level clouds. i) Lagrangian trajectory: initialized at the western edge of the cloud street at 13 UTC and subsequently advected by time-evolving wind fields based on the hourly ERA5 wind data (e.g., red lines in Fig. 1). ii) Instantaneous trajectory: initialized at the western edge of the cloud street and subsequently advected by a time-invariant ERA5 wind field fixed at the time of the GOES-16 snapshot (e.g., black lines in Fig. 1). As evident during the MCAO event on 24 January 2021 (Fig. 1), the close proximity between the Lagrangian trajectories and the instantaneous trajectories supports the validity of this 'space-time exchange' approach, in which a time-evolving evolution is represented by a trace in the spatial dimension at a given time.

135 2.5 Case selection

Essentially, the validity of 'space-time exchange' hinges on whether the timescale of the process of investigation (τ_{proc}) is much shorter than the timescale of large-scale meteorology evolution (τ_{met}) (Feingold et al., 2025). In our case, the slowly-evolving, relatively persistent boundary layer wind field and spatial gradients in large-scale meteorological conditions (i.e., SST, surface fluxes, and free-tropospheric subsidence) throughout the MCAO event are key underlying conditions that suffice this requirement. Based on this prerequisite of the 'space-time exchange' approach, we screen MCAO events occurred during ACTIVATE winter deployments between 2020-2022 for these large-scale conditions, yielding five events for further investigation (dates shown in Table 1). These cases are included in the library of MCAO events surveyed recently by Tornow et al. (2025). Moreover, these five events are identified as strong cases for Lagrangian modeling case studies based on a set of criteria surveyed in Tornow et al. (2025). All five events show the presence of liquid and frozen hydrometeors, as well as the presence of drizzle-and rain-sized particles (Tornow et al., 2025). Further contextual large-scale meteorological conditions during these MCAO events are described in Table 2 of Sorooshian et al. (2023) and characterized in Tornow et al. (2025).

For each event, seven GOES-16 snapshots at the top of each hour between 14–20 UTC (9–15 local time) are analyzed to investigate the cloud transition (Fig. 2). To characterize the mean transition within each snapshot, five closely aligned (separated by a 0.1° increment in both latitude and longitude) 12-hr instantaneous trajectories are generated, initialized at the western edge of the cloud street with their locations manually selected to overlap with ACTIVATE Air flight paths (locations detailed in Table 1; see also Fig. S1 for flight path and instantaneous trajectories overlaid on GOES-16 snapshots). Figure 2 shows the GOES-16 0.65 µm reflectance along the instantaneous trajectories at the top of each hour between 14–20 UTC for the five MCAO events (7 snapshots per event). Rather persistent patterns of cloud transition throughout sunlit hours are observed, except for the 11





January 2022 case where an extended overcast cloud deck, or a delayed cloud breakup, is evident later in the day (Fig. 2). GOES-16 retrieved cloud properties and ERA5 meteorological fields within a 1° by 1° area centered at each point along the trajectory are averaged across the 5 spatially separated starting points and across the 7 snapshots at the top of each hour during daytime to characterize the mean evolution of each event. Cloud properties are averaged among cloudy pixels (liquid or ice), except for domain-mean LWP and IWP which are averaged among all pixels within the 1° by 1° area. Water (ice) cloud fraction is calculated as the fraction of pixels within the 1° by 1° area that are identified as either 'water (ice)' or 'suspected water (ice)'.

160 3 Cloud transition

The clouds embedded in mid-latitude MCAO events off the east coast of North America typically undergo substantial boundary layer deepening as air masses move offshore across the Gulf Stream (GS), marked by increasing SST, buoyancy flux, cloud LWP, and cloud top height (CTH), as well as the emergence of frozen hydrometeors (e.g., Chellappan et al., 2024; Tornow et al., 2021, and Figs. 3-7). Given the large-scale meteorological gradients along the trajectory (Fig. 7), traces in the LWP- N_d space (Fig. 3), the domain-LWP versus domain-IWP space (Fig. 4), and the albedo versus cloud fraction space (Fig. 6) contain valuable information about the underlying boundary layer and microphysical (liquid and mixed-phase) processes that govern the cloud transition.

3.1 Liquid phase—LWP- $N_{ m d}$

A common feature among the five MCAO cases is the cloud thickening stage supported by the strengthening of buoyancy flux as the air moves across the GS to warmer ocean surfaces. This stage is marked by increases in both cloud LWP and droplet number 170 concentration (Fig. 3b). A key feature of the LWP-N_d phase space is the inference of cloud microphysical processes using isolines of r_e calculated by invoking the (sub)adiabatic assumption for stratiform warm clouds (e.g., Glassmeier et al., 2019; Zhang et al., 2022; Goren et al., 2022). In particular, the r_e isoline of $\sim 15 \, \mu m$ marks the transition from a non-precipitating regime to a precipitating regime through collision-coalescence and accretion processes (Gerber, 1996; vanZanten et al., 2005). Furthermore, one can underpin cloud processes based on the directionality of a trace in this space. These include microphysical processes: (i) droplet activation, marked by increases in LWP and N_d at constant r_e (i.e., along an r_e isoline; arrow 1 in Fig. 3a); (ii) condensational growth, marked by an increase in LWP at constant $N_{\rm d}$ (arrow 2); (iii) collision-coalescence, marked by a decrease in $N_{\rm d}$ at constant LWP (arrow 3); (iv) precipitation and evaporation, marked by decreases in both $N_{\rm d}$ and LWP (arrow 4); and (v) entrainment-mixing, marked by a decrease in LWP, with directionality depending on whether the mixing is homogeneous (along constant N_d , arrow 5.1) or inhomogeneous (along constant r_e , arrow 5.2). We note that these directionalities (arrows) are intended to conceptually indicate the dominant characteristics of a given process, while secondary effects such as dilution during entrainment mixing are neglected. It is evident that based on the directionality of the traces, these clouds have gone through a combination of droplet activation and condensational growth during the cloud thickening stage, as indicated by the gray symbols in Figure 3b. These two processes (arrow 1 and 2), driven by the increasing SST and buoyancy flux, together grow the clouds to their maxima in water condensate and shortwave albedo (Fig. 3b and c). 185



195

205

210

215



The process of water condensing onto existing droplets leads to larger cloud droplets (arrow 2), which increases the like-lihood of the collision-coalescence process that will decrease $N_{\rm d}$ (arrow 3). This microphysical transition is evident in all 5 MCAO cases investigated here (Fig. 3b). Larger droplet sizes reduce the total water surface area available to reflect incoming photons, making clouds less reflective of shortwave radiation at a given LWP and thereby causing a steeper decline in cloud albedo as LWP reduces (Fig. 3c). The breakup of overcast, closed-cell cloud fields, indicated by the transition from filled to open symbols in Figure 3b, occurs at $r_{\rm e}$ between 14-16 μ m for all cases, except on 29 March 2022, where the breakup took place later at larger $r_{\rm e}$ (trace marked by stars). The event on 29 March 2022 is marked by the highest peak- $N_{\rm d}$ (colors in Fig. 3c) and lowest peak-LWP among the 5 cases. A delayed closed-to-open transition with elevated droplet number concentration is consistent with those observed and simulated for the stratocumulus-to-cumulus transition over the eastern subtropical oceans (e.g., Yamaguchi et al., 2017; Goren et al., 2019; Christensen et al., 2020). If one sets aside the difference between large-scale meteorological conditions of these events, a negative correlation between peak-LWP and peak- $N_{\rm d}$ is found, consistent with the satellite-observed relationship between LWP and $N_{\rm d}$ (Gryspeerdt et al., 2019a; Zhang et al., 2022) and the entrainment feedbacks in non-precipitating warm clouds (Wang et al., 2003; Xue and Feingold, 2006; Bretherton et al., 2007; Hoffmann et al., 2020; Chen et al., 2024; Zhang et al., 2024).

200 3.2 Mixed phase—LWP-IWP

As the MBL deepens and clouds thicken, cloud top height rises while temperatures drop below freezing. This often leads to the formation of frozen hydrometeors, occurring approximately when the cloud attains its maximum LWP (colored symbols in Fig. 3b). Given the formation of ice, mixed-phase processes, such as the growth of ice particles at the expense of liquid condensate, complicate the interpretation of trace-directionality in liquid-only phase spaces (i.e., LWP- N_d and albedo-LWP). Therefore, we further investigate the directionality of traces in the domain-LWP versus domain-IWP space to infer mixed-phase processes.

Figure 4 zooms into the mixed-phase stage of cloud evolution, depicting traces in LWP-IWP space beginning with the first appearance of frozen hydrometeors (domain IWP > 1 g m⁻²; colored symbols in Fig. 3b). Given that GOES-16 retrievals assign a single cloud type to each pixel, we analyze domain-mean LWP and IWP, instead of in-cloud values, to characterize the 'mixed'-phase condition as a domain-level property rather than at the column or pixel level. Figures 3 and 4 share the same symbol conventions, and symbol size represents N_d and color denotes cloud top temperature in Figure 4. Among the five MCAO cases, two distinct types of traces emerge (magenta versus black in Fig. 4): (a) in the magenta group, ice forms at the expense of liquid, while (b) in the black group, ice and liquid grow simultaneously at first, after which ice continues to grow while liquid begins to decline rapidly. Not only the directionality of the traces, but also the rates of ice and liquid evolution are distinct between the two groups, yet consistent within each group. Despite the differences in large-scale meteorological conditions (Fig. 7), which affects the critical LWP at which ice starts to form (Fig. 3b and 4), ice growth depletes liquid at a similar rate in the magenta group, and slower than the black group. This slow depletion of liquid suggests the prevalence of a diffusional process where water vapor migrates from droplets to ice through evaporation and deposition, known as the Wegener-Bergeron-Findeisen (WBF) process (Wegener, 1912; Bergeron, 1935; Findeisen, 1938). In contrast, the black group is characterized by rapid liquid depletion preceded by the co-growth of ice and liquid, a distinctive feature of riming where



235

240

250



existing ice particles collect droplets through collisional freezing (Pruppacher and Klett, 2010; Tornow et al., 2021). The existence of riming in the black group is further supported by the coldest cloud-top temperatures (symbol colors in Fig. 4 and Fig. 7c), which favor the presence of abundant supercooled liquid water, and by the highest LWP (Figs. 3b and 4), which accelerates the riming rate (Pruppacher and Klett, 2010). Furthermore, cases in the black group are the cleanest (least N_d) among the five (Fig. 3b and c), which are the easiest to maintain a relatively high supersaturation, a condition that favors the co-growth of liquid and ice. In addition, exemplary 2DS ice habit images from samples during the above-cloud-base (ACB) leg in Figure 5 indicate rimed ice (in the form of aggregates and graupel) in the black group towards the beginning of transition, whereas the magenta group contains crystal-shaped particles (in the form of columns or dendrites). We note, however, that rimed ice is found ubiquitously later in the transition across all five cases, suggesting a typical taking-over by riming in these mid-latitude MCAO events (Tornow et al., 2025; Chellappan et al., 2024). Given that rates at which liquid and ice evolve also depend on height, updraft speed, and ice-liquid partitioning Ervens et al. (2011), instead of parsing individual processes, we here use trace directionality in satellite-derived GV spaces to identify fingerprints of the prevailing processes.

We note that frozen hydrometeors do not always emerge when cloud LWP is at its highest (Fig. 3b). Besides the co-growth of liquid and ice evident in the black group (Fig. 4), the 29 January 2021 event is distinguished by the warmest cloud tops among the five cases, resulting in a delayed onset of ice formation. In this case, liquid droplets had already begun to deplete, likely through warm-phase processes such as sedimentation and accretion. In general, for mixed-phase clouds governed either by the slower, diffusional growth process (magenta group) or the nonlinear, collisional grow process (black group), a higher LWP at the onset of ice formation typically leads to a subsequent higher IWP (Fig. 4).

3.3 Cloud breakup—albedo-cloud fraction (CF)

The shortwave albedo of a cloudy scene scales almost linearly with cloud fraction for warm clouds, especially warm stratiform clouds (Bender et al., 2011; Engström et al., 2015; Bender et al., 2017). It becomes increasingly nonlinear when the convective cloud regime is included (Feingold et al., 2016, 2017; McCoy et al., 2017, 2023). For mixed-phase clouds, at a given cloud fraction, the scene-albedo is governed by the liquid-ice partition of the cloud, as a result of the contrasting shortwave (SW) transmissivity between ice and liquid. Therefore, the albedo-CF scaling in mixed-phase clouds is expected to be nonlinear as well. Indeed we observe nonlinear behavior as the overcast cloud field breaks up in Figure 6, which zooms into the broken stage of MCAO evolution (beginning from the open symbols). In particular, distinguishable albedo-CF scaling is evident between the magenta (triangle, star, and square symbols) and black (upside-down triangle and circle symbols) groups (as categorized in Fig. 4), with the magenta group showing a steeper scaling between albedo and cloud fraction. This is consistent with the process fingerprints evident in Figure 4, where the faster depletion of liquid condensate (the key lever for cloud albedo) in the black group, driven by collisional freezing, supports the rapid decline in scene albedo. In addition, the continued growth of frozen hydrometeors after breakup, evident only in the black group (Fig. 4), further contributes to the decline in scene albedo. Counter to the rationale of the *Twomey* effect, where higher N_d leads to brighter clouds (Twomey, 1974, 1977), we observe the opposite where the spread in albedo is anti-correlated with N_d (color of the trace in Fig. 6). This is because the anti-correlation between peak-LWP and peak- N_d evident in these MCAO cases as discussed in Sec. 3.1 (Fig. 3b). Overall, we find a substantial spread



260

265

270

280

285



in scene albedo, and thus in cloud radiative effect (CRE), during the transition to a broken cloud field (Fig. 6). This spread is governed primarily by domain-LWP and secondarily by domain-IWP, resulting in a highly nonlinear albedo-CF scaling when mixed-phase clouds are considered.

Traces of large-scale meteorological conditions during the five MCAO events exhibit similar patterns as the air mass moves offshore and downstream across the GS (Fig. 7), confirming the typical evolution of boundary-layer thermodynamic and dynamical structure that drives the overcast-to-broken cloud transition (Pithan et al., 2018; Abel et al., 2017; Murray-Watson et al., 2023). This evolution is characterized by an initial increase in SST and M-index, which are associated with buoyancy flux enhancement and boundary layer deepening that lifts the cloud tops to subfreezing temperatures. This is followed by the shallowing and warming of cloud tops, together with a weakening of buoyancy fluxes, as the transition progresses into a broken cloud field (Fig. 7). It remains unclear why the cloud top temperature stayed nearly constant during the cloud-thickening stage on 29 January 2021 (triangle). Removal of both frozen and liquid hydrometeors through precipitation typically follows the cloud breakup as part of the transition, which is more pronounced when cloud top temperature warms rapidly, such as during 29 January 2021 (triangle) and 18 January 2022 (square) (Fig. 4).

4 Discussion

The 'space-time exchange' approach offers an effective and efficient way to characterize cloud transition from different perspectives. Here we take the advantage of the temporal coverage of GOES-16 satellite and examine the daytime evolution of the transition (Sect. 4.1). We then further characterize the transition in the form of cloud morphological organization (Sect. 4.2).

4.1 Daytime evolution of cloud transition

Instead of characterizing the transition from a Lagrangian perspective, we examine the evolution of instantaneous trajectories between 14–20 UTC (9–15 local time) using GOES-16, for reasons discussed in Section 2.4. Figure 8 shows the traces in LWP- N_d (left column), cloud-top height versus temperature (middle column), and buoyancy flux versus M-index (right column) spaces, as a function of time (colors). Overall, traces in LWP- N_d space exhibit similar patterns of evolution throughout the day for each event (Fig. 8 left). During the cloud-thickening stage, however, more noticeable differences emerge, also evident in cloud-top characteristics (Fig. 8 middle). This difference is marked by a cyclic pattern centered around local noon, with a clear directionality in r_e : traces around noon (yellow-ish) tend to begin with larger r_e (i.e., higher LWP and lower N_d), compared to morning (green) and late afternoon (red). A similar but skewed cyclic pattern is observed in cloud-top properties, with warmer cloud tops at a given height during late sunlit hours (Fig. 8middle), accompanied by a gradual increase in buoyancy flux and M-index throughout the day (Fig. 8right). Moreover, noon-time traces in LWP- N_d space suggest the co-occurrence of droplet activation and entrainment mixing (arrows 1 and 5 in Fig. 3a) during the cloud-thickening stage (e.g., 1 March 2020, 29 January 2021, and 29 March 2022; Fig. 8left).

This daytime evolution in the developing stage of MCAO subsequently leads to a similar cyclic pattern in the albedo-CF scaling (not shown) and in the timing of cloud breakup (open circles in Fig. 8), with cloud transitions occurring later (or farther



295

300

305

310

315



downstream) in near-noon traces. This delayed transition is likely driven by entrainment mixing during cloud-thickening, evident around noon, which reduces droplet size and thereby prolongs the time required to form sufficiently large drops for collisional processes (e.g., Yamaguchi et al., 2017; Goren et al., 2019), given that all five events are primarily precipitation-driven (liquid and ice) cloud transitions (Tornow et al., 2025). These findings underscore the important role of solar heating in modulating cloud evolution during sunlit hours (e.g., Zhang et al., 2024; Chen et al., 2024).

4.2 Evolution of cloud morphology and organization

The cloud radiative effect is closely tied to cloud morphology and the organization of the cloud field, such as the self-aggregation patterns found in trade cumulus (Bony et al., 2020; Eastman et al., 2024) and the precipitation-driven oscillation between open- and closed-cellular structures in marine stratocumulus (Wang and Feingold, 2009; Feingold et al., 2010; Glassmeier and Feingold, 2017). For marine warm clouds, distinct cloud albedo-fraction relationships have been observed for different mesoscale cloud morphologies (McCoy et al., 2023). As discussed in Section 3, this relationship is further influenced by mixed-phase microphysical processes, given the strong dependence of shortwave reflectivity on hydrometeor phase (Fig. 6). Wu and Ovchinnikov (2022) investigated the evolution of cloud morphological properties during two Arctic cold-air-outbreaks using a watershed approach applied to satellite observations, and found a convergence in the scaling between 'cloud size' and 'nearest-neighbor distance' (the distance between two adjacent cloud objects) as the cloud field transitions into cellular structures.

Here we examine cloud organizational evolution during the overcast-to-broken transition as described by a measure of deviation from randomness, following Koren et al. (2024). Essentially, this approach assesses the departure of a given 2D cloud field from a predefined, "perfectly" random cloud field constructed using a Bernoulli random matrix (Papoulis, 1984). Specifically, a cloud field is first converted into a binary cloud mask based on a τ_c threshold of 5. The distributions of cloudchord length (analogous to cloud size) and void-chord length (analogous to nearest-neighbor distance) in this binary mask are then compared against those from a random cloud mask, which is defined by a single parameter, the observed cloud fraction calculated from the original cloud field. This comparison yields a Goodness-of-Fit score based on the Kolmogorov-Smirnov (KS) test (Justel et al., 1997), defining the deviation from randomness, which ranges from 0 (perfectly random) to 1. Figure 9 depicts the evolution in cloud organization since the transition as a function of cloud fraction, with cases colored by minimum cloud top temperature. The degree of organization (or deviation from randomness) in cloud size (or cloud-chord length) scales linearly with CF (Fig. 9a), whereas organization in void size (or nearest-neighbor distance) remains largely invariant throughout the transition (Fig. 9b). The scaling between cloud-size organization and CF is slightly separated by cloud-top temperature, such that the coldest (and highest) cloud tops are associated with the highest degree of organization and highest scene albedo during the transition (Figs. 6-7 and 9). Nevertheless, the degree of organization in both cloud size and void size converges to a common range of 0.3-0.4 (Fig. 9a and b), despite differences in boundary layer thermodynamic and dynamical structures, $N_{\rm d}$, LWP, IWP, CRE, and even the visual pattern of the cloud field (Figs. 3-7, and 9c-e). This convergence is consistent with the findings of Wu and Ovchinnikov (2022). We note a relatively large spread in cloud organization under high cloud-fraction conditions (CF > 0.9; Fig. 9a-c). This is likely due to the $2^{\circ} \times 2^{\circ}$ cloud-mask domain, which inevitably includes a mixture of





overcast and broken conditions. In addition, the τ_c -based cloud mask is particularly sensitive to the domain ice fraction, which varies considerably across the five events (Figs. 3-4).

5 Conclusions

325

330

340

345

350

Boundary layer clouds embedded in marine cold-air outbreaks are recognized by their characteristic morphological evolution, transitioning from overcast, stratiform clouds to broken, cumuliform cloud field downwind. The timing of this transition, along with the frequent coexistence of frozen and liquid hydrometeors, gives MCAO clouds substantial leverage in modulating the top-of-atmosphere radiation budget. This characteristic evolution remains a challenge for models to capture due to the multi-scale nature of MCAO events and the intricate interactions among hydrometeors of different phases. Airborne in-situ measurements provide rich detail on the micro- and macro-physical evolution of the cloud field, but are constrained by the limited range of deployed aircraft. Geostationary satellites, in contrast, offer extensive spatiotemporal coverage but provide only two-dimensional views, limiting their utility for process-level inference. To overcome these limitations, this study introduces an innovative 'space-time exchange' framework that generates instantaneous trajectories from individual satellite snapshots (Figs. 1-2). These trajectories are then used to infer the warm- and mixed-phase microphysical processes governing the overcast-to-broken cloud transition by tracking evolution in carefully selected geophysical variable spaces that target liquid-phase, mixed-phase, and cloud breakup, individually.

Using this framework, we investigate five MCAO events, all sampled by the NASA ACTIVATE field campaign between 2020-2022. The findings on the processes influencing cloud transitions are summarized as follows:

- Precipitation driven cloud transition, further facilitated by processes involving frozen hydrometeors, is evident in all five events. Clear directionality of traces in LWP-N_d space indicate a progressing dominance of different warm-phase processes, from droplet activation to condensational growth to collision-coalescence, during the cloud-thickening stage (Fig. 3).
- 2. Setting aside subtle differences in large-scale meteorological conditions, a negative correlation between peak-LWP and peak- $N_{\rm d}$ is observed across the five cases, consistent with entrainment feedbacks in non-precipitating warm clouds. Elevated $N_{\rm d}$ also leads to a delayed close-to-open transition in one of the five MCAO cases (Fig. 3).
- 3. Fingerprints of two distinct mixed-phase processes are identified using the LWP-IWP space: (i) a diffusional process that migrates vapor from liquid to ice depletes water condensate at a slow, steady pace (suggesting WBF); (ii) a collisional freezing process that depletes water rapidly and is preceded by a co-growth of ice and liquid (suggesting riming) (Fig. 4).
 - 4. We found a large spread in the nonlinear scaling between albedo and cloud fraction among the five events. They also exhibit two distinct behaviors apparently tied to features in mixed-phase process, with the collisional freezing process exhibiting a sharper decline of albedo (Fig. 6).



360

365

375



- 5. Daytime evolution of cloud transition indicates a cyclic pattern centered around noon, at which cloud transition is marked by delayed breakup driven by reduced droplet size and evident entrainment processes (Fig. 8).
- 6. Cloud organizational evolution, depicted in the form *deviation from randomness*, converges among five cases, despite differences in cloud micro- and macro-physical properties and in boundary layer characteristics (Fig. 9).

These findings stress the critical need to accurately represent both warm- and cold-phase microphysical processes in models, in order to characterize the intricate cloud transition during mixed-phase MCAO events, whose potential role as a negative cloud-feedback agent remains to be determined.

This novel 'space-time exchange' framework, combined with the selected GV spaces, has the potential to be applied in Lagrangian modeling and modeling-observation synergy studies to benchmark process fingerprints using parcel models or to characterize process importance using perturbation experiments. Moreover, a hierarchy of modeling studies (e.g., Chen et al., 2022; Li et al., 2022, 2023; Tang et al., 2024; Tornow et al., 2021, 2023) conducted as part of the NASA ACTIVATE mission could be gathered and compared within the same geophysical variable spaces illustrated in this work, enabling an assessment of the fidelity of their process representations. Beyond the field campaign period, this framework also provides a means to characterize long-term trends in MCAO cloud evolution and radiative impacts over this region, in light of substantial regional changes in aerosol loading (Sorooshian et al., 2020) and SST in recent decades (Park et al., 2024).

Leveraging the persistent large-scale meteorological gradients that characterize MCAO events, we have demonstrated the usefulness of the 'space-time exchange' approach by exploiting the extensive spatial coverage of satellite observations. While unambiguous parsing of processes remains challenging with this method, it effectively captures fingerprints of dominant processes over the spatial dimension of satellite snapshots and underscores the potential of space-time exchange for process inference (Feingold et al., 2025). The inferred process fingerprints serve as an additional line of evidence from the satellite perspective, complementing existing modeling and in-situ characterizations of mixed-phase processes during mid-latitude MCAOs (Tornow et al., 2021, 2023, 2025; Chellappan et al., 2024).

Data availability. The ACTIVATE data, including GOES-16 retrievals, are are publicly archived on NASA's Atmospheric Science Data Center (ASDC) Distributed Active Archive Center (DAAC; https://doi.org/10.5067/SUBORBITAL/ACTIVATE/DATA001) and are accessible via https://asdc.larc.nasa.gov/project/ACTIVATE. The fifth-generation ECMWF (ERA5) atmospheric reanalyses of the global climate data were obtained from the Copernicus Climate Change Service at https://cds.climate.copernicus.eu/ (Hersbach et al., 2020), and are accessible via https://doi.org/10.24381/cds.6860a573 and https://doi.org/10.24381/cds.f17050d7.

Author contributions. JZ conceived the ideas, carried out the data analysis, and wrote the first draft. DP provided the GOES-16 cloud retrievals. TD provided the code for characterizing cloud organization. All authors contributed to writing and editing.



385



380 *Competing interests.* Two of the authors are members of the editorial board of Atmospheric Chemistry and Physics. Other than this, the authors declare that they have no conflict of interests.

Acknowledgements. The work was funded by ACTIVATE, a NASA Earth Venture Suborbital-3 (EVS-3) investigation funded by NASA's Earth Science Division and managed through the Earth System Science Pathfinder Program Office. GF and JZ acknowledge support from the NASA ACTIVATE program under Reimbursable Agreement number NNL23OB04A. DP also acknowledges the support of the CERES program. AS acknowledges support from NASA grant no. 80NSSC19K0442. TD was supported by the CIRES Visiting Fellows Program and the NOAA Cooperative Agreement with CIRES, NA17OAR4320101. JSL acknowledges support from the NOAA Cooperative Agreement with CIRES, NA17OAR4320101, and the U.S. Department of Commerce, Earth's Radiation Budget grant, NOAA CPO Climate & CI #03-01-07-001.





References

395

- Abel, S. J., Boutle, I. A., Waite, K., Fox, S., Brown, P. R. A., Cotton, R., Lloyd, G., Choularton, T. W., and Bower, K. N.: The Role of Precipitation in Controlling the Transition from Stratocumulus to Cumulus Clouds in a Northern Hemisphere Cold-Air Outbreak, Journal of the Atmospheric Sciences, 74, 2293–2314, https://doi.org/10.1175/JAS-D-16-0362.1, 2017.
 - Albrecht, B. A., Bretherton, C. S., Johnson, D., Scubert, W. H., and Frisch, A. S.: The Atlantic Stratocumulus Transition Experiment—ASTEX, Bulletin of the American Meteorological Society, 76, 889–904, https://doi.org/10.1175/1520-0477(1995)076<0889:TASTE>2.0.CO;2, 1995.
 - Bellouin, N., Quaas, J., Gryspeerdt, E., Kinne, S., Stier, P., Watson-Parris, D., Boucher, O., Carslaw, K., Christensen, M., Daniau, A.-L., Dufresne, J.-L., Feingold, G., Fiedler, S., Forster, P., Gettelman, A., Haywood, J., Lohmann, U., Malavelle, F., Mauritsen, T., and Stevens, B.: Bounding global aerosol radiative forcing of climate change, Rev. of Geophys., 58, e2019RG000660, https://doi.org/10.1029/2019RG000660, 2020.
- Bender, F. A.-M., Charlson, R. J., Ekman, A. M. L., and Leahy, L. V.: Quantification of Monthly Mean Regional Scale Albedo of Marine Stratiform Clouds in Satellite Observations and GCMs, J. Appl. Meteor. Climatol., 50, 2139–2148, https://doi.org/10.1175/JAMC-D-11-049.1, 2011.
 - Bender, F. A.-M., Engström, A., Wood, R., and Charlson, R. J.: Evaluation of Hemispheric Asymmetries in Marine Cloud Radiative Properties, Journal of Climate, 30, 4131–4147, https://doi.org/10.1175/JCLI-D-16-0263.1, 2017.
- Bennartz, R.: Global assessment of marine boundary layer cloud droplet number concentration from satellite, J. Geophys. Res. Atmos., 112, https://doi.org/10.1029/2006JD007547, 2007.
 - Bergeron, T.: On the Physics of Cloud and Precipitation, in: Proceedings of the 5th Assembly of the International Union of Geodesy and Geophysics (IUGG), vol. 2, pp. 156–178, Lisbon, 1935.
- Boltzmann, L.: Ueber die Eigenschaften monozyklischer und damit verwandter Systeme des zweiten Hauptsatzes der Wärmetheorie, Wissenschaftliche Abhandlungen, 3, 122–152, 1884.
 - Bony, S., Schulz, H., Vial, J., and Stevens, B.: Sugar, Gravel, Fish, and Flowers: Dependence of Mesoscale Patterns of Trade-Wind Clouds on Environmental Conditions, Geophysical Research Letters, 47, https://doi.org/10.1029/2019GL085988, 2020.
 - Bretherton, C. S.: A conceptual model of the stratocumulus-trade-cumulus transition in the subtropical oceans, Proceeding of the 11th International Conference on Clouds and Precipitation, vol. 1, pp. 374–377, 1992.
- Bretherton, C. S. and Wyant, M. C.: Moisture Transport, Lower-Tropospheric Stability, and Decoupling of Cloud-Topped Boundary Layers, J. Atmos. Sci., 54, 148–167, https://doi.org/10.1175/1520-0469(1997)054<0148:MTLTSA>2.0.CO;2, 1997.
 - Bretherton, C. S., Blossey, P. N., and Uchida, J.: Cloud droplet sedimentation, entrainment efficiency, and subtropical stratocumulus albedo, Geophys. Res. Lett., 34, L03 813, https://doi.org/https://doi.org/10.1029/2006GL027648, 2007.
- Brümmer, B.: Boundary-layer modification in wintertime cold-air outbreaks from the Arctic sea ice, Boundary-Layer Meteorology, 80, 109–125, https://doi.org/https://doi.org/10.1007/BF00119014, 1996.
 - Brümmer, B.: Roll and Cell Convection in Wintertime Arctic Cold-Air Outbreaks, Journal of the Atmospheric Sciences, 56, 2613–2636, https://doi.org/https://doi.org/10.1175/1520-0469(1999)056<2613:RACCIW>2.0.CO;2, 1999.
 - Chellappan, S., Zuidema, P., Kirschler, S., Voigt, C., Cairns, B., Crosbie, E. C., Ferrare, R., Hair, J., Painemal, D., Shingler, T., Shook, M., Thornhill, K. L., Tornow, F., and Sorooshian, A.: Microphysical Evolution in Mixed-Phase Midlatitude Marine Cold-Air Outbreaks, Journal of the Atmospheric Sciences, 81, 1725–1747, https://doi.org/10.1175/JAS-D-23-0203.1, 2024.



435



- Chen, J., Wang, H., Li, X., Painemal, D., Sorooshian, A., Thornhill, K. L., Robinson, C., and Shingler, T.: Impact of Meteorological Factors on the Mesoscale Morphology of Cloud Streets during a Cold-Air Outbreak over the Western North Atlantic, Journal of the Atmospheric Sciences, 79, 2863–2879, https://doi.org/10.1175/JAS-D-22-0034.1, 2022.
- Chen, Y.-S., Zhang, J., Glassmeier, F., Hoffmann, F., Yamaguchi, T., Zhou, X., and Feingold, G.: Diurnal evolution of non-precipitating stratocumuli in an LES ensemble, EGUsphere, 2024, 1–42, https://doi.org/10.5194/egusphere-2024-1033, 2024.
 - Christensen, M. W., Jones, W. K., and Stier, P.: Aerosols enhance cloud lifetime and brightness along the stratus-to-cumulus transition, P. Natl. Acad. Sci. USA, 117, 17591–17598, https://doi.org/10.1073/pnas.1921231117, 2020.
 - de Roode, S. R., Frederikse, T., Siebesma, A. P., Ackerman, A. S., Chylik, J., Field, P. R., Fricke, J., Gryschka, M., Hill, A., Honnert, R., Krueger, S. K., Lac, C., Lesage, A. T., and Tomassini, L.: Turbulent Transport in the Gray Zone: A Large Eddy Model Intercomparison Study of the CONSTRAIN Cold Air Outbreak Case, Journal of Advances in Modeling Earth Systems, 11, 597–623, https://doi.org/10.1029/2018MS001443, 2019.
 - Eastman, R., McCoy, I. L., Schulz, H., and Wood, R.: A survey of radiative and physical properties of North Atlantic mesoscale cloud morphologies from multiple identification methodologies, Atmospheric Chemistry and Physics, 24, 6613–6634, https://doi.org/10.5194/acp-24-6613-2024, 2024.
- Engström, A., Bender, F. A., Charlson, R. J., and Wood, R.: The nonlinear relationship between albedo and cloud fraction on near-global, monthly mean scale in observations and in the CMIP5 model ensemble, Geophysical Research Letters, 42, 9571–9578, https://doi.org/10.1002/2015GL066275, 2015.
 - Ervens, B., Feingold, G., Sulia, K., and Harrington, J.: The impact of microphysical parameters, ice nucleation mode, and habit growth on the ice/liquid partitioning in mixed-phase Arctic clouds, Journal of Geophysical Research, 116, https://doi.org/10.1029/2011JD015729, 2011
 - Feingold, G., Koren, I., Wang, H., Xue, H., and Brewer, W. A.: Precipitation-generated oscillations in open cellular cloud fields, Nature, 466, 849–852, https://doi.org/10.1038/nature09314, 2010.
 - Feingold, G., McComiskey, A., Yamaguchi, T., Johnson, J. S., Carslaw, K. S., and Schmidt, K. S.: New approaches to quantifying aerosol influence on the cloud radiative effect, Proc. Natl. Acad. Sci., 113, 5812–5819, https://doi.org/10.1073/pnas.1514035112, 2016.
- Feingold, G., Balsells, J., Glassmeier, F., Yamaguchi, T., Kazil, J., and McComiskey, A.: Analysis of albedo versus cloud fraction relationships in liquid water clouds using heuristic models and large eddy simulation, Journal of Geophysical Research: Atmospheres, 122, 7086–7102, https://doi.org/10.1002/2017JD026467, 2017.
 - Feingold, G., Glassmeier, F., Zhang, J., and Hoffmann, F.: Opinion: Inferring Process from Snapshots of Cloud Systems, Atmos. Chem. Phys., accepted, 1–28, https://doi.org/10.5194/egusphere-2025-1869, 2025.
- 455 Findeisen, W.: Kolloid-meteorologische Vorgänge bei Niederschlagsbildung, Meteorologische Zeitschrift, 55, 121–133, 1938.
 - Fletcher, J., Mason, S., and Jakob, C.: The Climatology, Meteorology, and Boundary Layer Structure of Marine Cold Air Outbreaks in Both Hemispheres, Journal of Climate, 29, 1999–2014, https://doi.org/10.1175/JCLI-D-15-0268.1, 2016a.
 - Fletcher, J. K., Mason, S., and Jakob, C.: A Climatology of Clouds in Marine Cold Air Outbreaks in Both Hemispheres, Journal of Climate, 29, 6677–6692, https://doi.org/10.1175/JCLI-D-15-0783.1, 2016b.
- Forster, P., Storelvmo, T., Armour, K., Collins, W., Dufresne, J.-L., Frame, D., Lunt, D. J., Mauritsen, T., Palmer, M. D., Watanabe, M., Wild, M., and Zhang, H.: The Earth's Energy Budget, Climate Feedbacks, and Climate Sensitivity, in: Climate Change 2021: The Physical Science Basis, Contribution of Working Group I to the Sixth Assessment Report of the Intergovernmental Panel on Climate Change, edited by Masson-Delmotte, V., Zhai, P., Pirani, A., Connors, S. L., Péan, C., Berger, S., Caud, N., Chen, Y., Goldfarb, L., Gomis, M. I.,





- Huang, M., Leitzell, K., Lonnoy, E., Matthews, J. B. R., Maycock, T. K., Waterfield, T., Yelekçi, O., Yu, R., and Zhou, B., pp. 923–1054, Cambridge University Press, Cambridge, United Kingdom and New York, NY, USA, 2021.
 - Gerber, H.: Microphysics of Marine Stratocumulus Clouds with Two Drizzle Modes, J. Atmos. Sci, 53, 1649–1662, https://doi.org/10.1175/1520-0469(1996)053<1649:MOMSCW>2.0.CO:2, 1996.
 - Glassmeier, F. and Feingold, G.: Network approach to patterns in stratocumulus clouds, Proceedings of the National Academy of Sciences, 114, 10578–10583, https://doi.org/10.1073/pnas.1706495114, 2017.
- Glassmeier, F., Hoffmann, F., Johnson, J. S., Yamaguchi, T., Carslaw, K. S., and Feingold, G.: An emulator approach to stratocumulus susceptibility, Atmos. Chem. Phys., 19, 10191–10203, https://doi.org/10.5194/acp-19-10191-2019, 2019.
 - Goren, T., Kazil, J., Hoffmann, F., Yamaguchi, T., and Feingold, G.: Anthropogenic Air Pollution Delays Marine Stratocumulus Breakup to Open Cells, Geophysical Research Letters, 46, 14 135–14 144, https://doi.org/10.1029/2019GL085412, 2019.
- Goren, T., Feingold, G., Gryspeerdt, E., Kazil, J., Kretzschmar, J., Jia, H., and Quaas, J.: Projecting Stratocumulus Transitions on the Albedo—Cloud Fraction Relationship Reveals Linearity of Albedo to Droplet Concentrations, Geophysical Research Letters, 49, https://doi.org/10.1029/2022GL101169, 2022.
 - Grosvenor, D. P. and Wood, R.: The effect of solar zenith angle on MODIS cloud optical and microphysical retrievals within marine liquid water clouds, Atmos. Chem. Phys., 14, 7291–7321, https://doi.org/10.5194/acp-14-7291-2014, 2014.
- Grosvenor, D. P., Sourdeval, O., Zuidema, P., Ackerman, A., Alexandrov, M. D., Bennartz, R., Boers, R., Cairns, B., Chiu, J. C., Christensen,
 M., Deneke, H., Diamond, M., Feingold, G., Fridlind, A., HÃŒnerbein, A., Knist, C., Kollias, P., Marshak, A., McCoy, D., Merk, D.,
 Painemal, D., Rausch, J., Rosenfeld, D., Russchenberg, H., Seifert, P., Sinclair, K., Stier, P., van Diedenhoven, B., Wendisch, M., Werner,
 F., Wood, R., Zhang, Z., and Quaas, J.: Remote Sensing of Droplet Number Concentration in Warm Clouds: A Review of the Current
 State of Knowledge and Perspectives, Rev. Geophys., 56, 409–453, https://doi.org/10.1029/2017RG000593, 2018.
- Gryspeerdt, E., Goren, T., Sourdeval, O., Quaas, J., Mülmenstädt, J., Dipu, S., Unglaub, C., Gettelman, A., and Christensen, M.: Constraining the aerosol influence on cloud liquid water path, Atmos. Chem. Phys., 19, 5331–5347, https://doi.org/10.5194/acp-19-5331-2019, 2019a.
 - Gryspeerdt, E., Smith, T. W. P., O'Keeffe, E., Christensen, M. W., and Goldsworth, F. W.: The Impact of Ship Emission Controls Recorded by Cloud Properties, Geophys. Res. Lett., 46, 12547–12555, https://doi.org/10.1029/2019GL084700, 2019b.
 - Hersbach, H., Bell, B., Berrisford, P., Hirahara, S., Horányi, A., Muñoz-Sabater, J., Nicolas, J., Peubey, C., Radu, R., Schepers, D., Simmons, A., Soci, C., Abdalla, S., Abellan, X., Balsamo, G., Bechtold, P., Biavati, G., Bidlot, J., Bonavita, M., De Chiara, G., Dahlgren, P., Dee,
- D., Diamantakis, M., Dragani, R., Flemming, J., Forbes, R., Fuentes, M., Geer, A., Haimberger, L., Healy, S., Hogan, R. J., Hólm, E., Janisková, M., Keeley, S., Laloyaux, P., Lopez, P., Lupu, C., Radnoti, G., de Rosnay, P., Rozum, I., Vamborg, F., Villaume, S., and Thépaut, J.-N.: The ERA5 global reanalysis, Q. J. Roy. Meteor. Soc., 146, 1999–2049, https://doi.org/10.1002/qj.3803, 2020.
 - Hoffmann, F., Glassmeier, F., Yamaguchi, T., and Feingold, G.: Liquid Water Path Steady States in Stratocumulus: Insights from Process-Level Emulation and Mixed-Layer Theory, J. Atmos. Sci., 77, 2203–2215, https://doi.org/10.1175/JAS-D-19-0241.1, 2020.
- Justel, A., Peña, D., and Zamar, R.: A multivariate Kolmogorov-Smirnov test of goodness of fit, Statistics & Probability Letters, 35, 251–259, https://doi.org/10.1016/S0167-7152(97)00020-5, 1997.
 - Karalis, M., Sotiropoulou, G., Abel, S. J., Bossioli, E., Georgakaki, P., Methymaki, G., Nenes, A., and Tombrou, M.: Effects of secondary ice processes on a stratocumulus to cumulus transition during a cold-air outbreak, Atmospheric Research, 277, 106302, https://doi.org/10.1016/j.atmosres.2022.106302, 2022.
- 500 Kirschler, S., Voigt, C., Anderson, B. E., Chen, G., Crosbie, E. C., Ferrare, R. A., Hahn, V., Hair, J. W., Kaufmann, S., Moore, R. H., Painemal, D., Robinson, C. E., Sanchez, K. J., Scarino, A. J., Shingler, T. J., Shook, M. A., Thornhill, K. L., Winstead, E. L., Ziemba,



525



- L. D., and Sorooshian, A.: Overview and statistical analysis of boundary layer clouds and precipitation over the western North Atlantic Ocean, Atmospheric Chemistry and Physics, 23, 10731–10750, https://doi.org/10.5194/acp-23-10731-2023, 2023.
- Klein, S. A. and Hartmann, D. L.: The Seasonal Cycle of Low Stratiform Clouds, J. Climate, 6, 1587–1606, https://doi.org/10.1175/1520-0442(1993)006<1587:TSCOLS>2.0.CO;2, 1993.
 - Kolstad, E. W. and Bracegirdle, T. J.: Marine cold-air outbreaks in the future: an assessment of IPCC AR4 model results for the Northern Hemisphere, Climate Dynamics, 30, 871–885, https://doi.org/10.1007/s00382-007-0331-0, 2008.
 - Koren, I., Dror, T., Altaratz, O., and Chekroun, M. D.: Cloud Versus Void Chord Length Distributions (LvL) as a Measure for Cloud Field Organization, Geophysical Research Letters, 51, https://doi.org/10.1029/2024GL108435, 2024.
- Li, X.-Y., Wang, H., Chen, J., Endo, S., George, G., Cairns, B., Chellappan, S., Zeng, X., Kirschler, S., Voigt, C., Sorooshian, A., Crosbie, E., Chen, G., Ferrare, R. A., Gustafson, W. I., Hair, J. W., Kleb, M. M., Liu, H., Moore, R., Painemal, D., Robinson, C., Scarino, A. J., Shook, M., Shingler, T. J., Thornhill, K. L., Tornow, F., Xiao, H., Ziemba, L. D., and Zuidema, P.: Large-Eddy Simulations of Marine Boundary Layer Clouds Associated with Cold-Air Outbreaks during the ACTIVATE Campaign. Part I: Case Setup and Sensitivities to Large-Scale Forcings, Journal of the Atmospheric Sciences, 79, 73–100, https://doi.org/10.1175/JAS-D-21-0123.1, 2022.
- Li, X.-Y., Wang, H., Chen, J., Endo, S., Kirschler, S., Voigt, C., Crosbie, E., Ziemba, L. D., Painemal, D., Cairns, B., Hair, J. W., Corral, A. F., Robinson, C., Dadashazar, H., Sorooshian, A., Chen, G., Ferrare, R. A., Kleb, M. M., Liu, H., Moore, R., Scarino, A. J., Shook, M. A., Shingler, T. J., Thornhill, K. L., Tornow, F., Xiao, H., and Zeng, X.: Large-Eddy Simulations of Marine Boundary Layer Clouds Associated with Cold-Air Outbreaks during the ACTIVATE Campaign. Part II: Aerosol–Meteorology–Cloud Interaction, Journal of the Atmospheric Sciences, 80, 1025–1045, https://doi.org/10.1175/JAS-D-21-0324.1, 2023.
- Martin, G. M., Johnson, D. W., and Spice, A.: The Measurement and Parameterization of Effective Radius of Droplets in Warm Stratocumulus Clouds, J. Atmos. Sci, 51, 1823–1842, https://doi.org/10.1175/1520-0469(1994)051<1823:TMAPOE>2.0.CO;2, 1994.
 - McCoy, I. L., Wood, R., and Fletcher, J. K.: Identifying Meteorological Controls on Open and Closed Mesoscale Cellular Convection Associated with Marine Cold Air Outbreaks, J. Geophys. Res.-Atmos., 122, 11,678–11,702, https://doi.org/10.1002/2017JD027031, 2017.
 - McCoy, I. L., McCoy, D. T., Wood, R., Zuidema, P., and Bender, F. A.: The Role of Mesoscale Cloud Morphology in the Shortwave Cloud Feedback, Geophysical Research Letters, 50, https://doi.org/10.1029/2022GL101042, 2023.
 - Minnis, P., Nguyen, L., Palikonda, R., Heck, P. W., Spangenberg, D. A., Doelling, D. R., Kirk Ayers, J., Smith, W. L., Khaiyer, M. M., Trepte, Q. Z., Avey, L. A., Chang, F.-L., Yost, C. R., Chee, T. L., and Szedung, T. L.: Near-real time cloud retrievals from operational and research meteorological satellites, Proc. SPIE 7107, Remote Sensing of Clouds and the Atmosphere XIII, 710703, https://doi.org/10.1117/12.800344, 2008.
- Minnis, P., Sun-Mack, S., Chen, Y., Chang, F.-L., Yost, C. R., Smith, W. L., Heck, P. W., Arduini, R. F., Bedka, S. T., Yi, Y., Hong, G., Jin, Z., Painemal, D., Palikonda, R., Scarino, B. R., Spangenberg, D. A., Smith, R. A., Trepte, Q. Z., Yang, P., and Xie, Y.: CERES MODIS Cloud Product Retrievals for Edition 4—Part I: Algorithm Changes, IEEE Transactions on Geoscience and Remote Sensing, 59, 2744–2780, https://doi.org/10.1109/TGRS.2020.3008866, 2021.
 - Murray-Watson, R. J., Gryspeerdt, E., and Goren, T.: Investigating the development of clouds within marine cold-air outbreaks, Atmospheric Chemistry and Physics, 23, 9365–9383, https://doi.org/10.5194/acp-23-9365-2023, 2023.
 - Painemal, D. and Zuidema, P.: Assessment of MODIS cloud effective radius and optical thickness retrievals over the southeast Pacific with VOCALS-REx in situ measurements, J. Geophys. Res.-Atmos., 116, 1–16, https://doi.org/10.1029/2011JD016155, 2011.
 - Painemal, D., Spangenberg, D., Smith Jr., W. L., Minnis, P., Cairns, B., Moore, R. H., Crosbie, E., Robinson, C., Thornhill, K. L., Winstead, E. L., and Ziemba, L.: Evaluation of satellite retrievals of liquid clouds from the GOES-13 imager and MODIS over the midlatitude North



545



- Atlantic during the NAAMES campaign, Atmospheric Measurement Techniques, 14, 6633–6646, https://doi.org/10.5194/amt-14-6633-2021, 2021.
 - Papoulis, A.: Bernoulli Trials, in: Probability, Random Variables, and Stochastic Processes, pp. 57-63, McGraw-Hill, 1984.
 - Park, J. M., McComiskey, A. C., Painemal, D., and Smith, W. L.: Long-Term Trends in Aerosols, Low Clouds, and Large-Scale Meteorology Over the Western North Atlantic From 2003 to 2020, Journal of Geophysical Research: Atmospheres, 129, https://doi.org/10.1029/2023JD039592, 2024.
 - Pithan, F., Svensson, G., Caballero, R., Chechin, D., Cronin, T. W., Ekman, A. M. L., Neggers, R., Shupe, M. D., Solomon, A., Tjernström, M., and Wendisch, M.: Role of air-mass transformations in exchange between the Arctic and mid-latitudes, Nature Geoscience, 11, 805–812, https://doi.org/10.1038/s41561-018-0234-1, 2018.
 - Platnick, S., King, M. D., Ackerman, S. A., Menzel, W. P., Baum, B. A., Riedi, J. C., and Frey, R. A.: The MODIS cloud products: algorithms and examples from Terra, IEEE Trans. Geos. Remote Sens., 41, 459–473, https://doi.org/10.1109/TGRS.2002.808301, 2003.
 - Pruppacher, H. and Klett, J.: Microphysics of Clouds and Precipitation, Springer Netherlands, ISBN 9780306481000, https://doi.org/10.1007/978-0-306-48100-0, 2010.
 - Quaas, J., Boucher, O., and Lohmann, U.: Constraining the total aerosol indirect effect in the LMDZ and ECHAM4 GCMs using MODIS satellite data, Atmospheric Chemistry and Physics, 6, 947–955, https://doi.org/10.5194/acp-6-947-2006, 2006.
- Sandu, I. and Stevens, B.: On the Factors Modulating the Stratocumulus to Cumulus Transitions, Journal of the Atmospheric Sciences, 68, 1865–1881, https://doi.org/10.1175/2011JAS3614.1, 2011.
 - Sandu, I., Stevens, B., and Pincus, R.: On the transitions in marine boundary layer cloudiness, Atmospheric Chemistry and Physics, 10, 2377–2391, https://doi.org/10.5194/acp-10-2377-2010, 2010.
- Sorooshian, A., Anderson, B., Bauer, S. E., Braun, R. A., Cairns, B., Crosbie, E., Dadashazar, H., Diskin, G., Ferrare, R., Flagan, R. C., Hair,

 J., Hostetler, C., Jonsson, H. H., Kleb, M. M., Liu, H., MacDonald, A. B., McComiskey, A., Moore, R., Painemal, D., Russell, L. M.,

 Seinfeld, J. H., Shook, M., Smith, W. L., Thornhill, K., Tselioudis, G., Wang, H., Zeng, X., Zhang, B., Ziemba, L., and Zuidema, P.:

 Aerosol–Cloud–Meteorology Interaction Airborne Field Investigations: Using Lessons Learned from the U.S. West Coast in the Design

 of ACTIVATE off the U.S. East Coast, Bulletin of the American Meteorological Society, 100, 1511–1528, https://doi.org/10.1175/BAMS
 D-18-0100.1, 2019.
- Sorooshian, A., Corral, A. F., Braun, R. A., Cairns, B., Crosbie, E., Ferrare, R., Hair, J., Kleb, M. M., Hossein Mardi, A., Maring, H., McComiskey, A., Moore, R., Painemal, D., Scarino, A. J., Schlosser, J., Shingler, T., Shook, M., Wang, H., Zeng, X., Ziemba, L., and Zuidema, P.: Atmospheric Research Over the Western North Atlantic Ocean Region and North American East Coast: A Review of Past Work and Challenges Ahead, Journal of Geophysical Research: Atmospheres, 125, https://doi.org/10.1029/2019JD031626, 2020.
- Sorooshian, A., Alexandrov, M. D., Bell, A. D., Bennett, R., Betito, G., Burton, S. P., Buzanowicz, M. E., Cairns, B., Chemyakin, E. V., Chen,
 G., Choi, Y., Collister, B. L., Cook, A. L., Corral, A. F., Crosbie, E. C., van Diedenhoven, B., DiGangi, J. P., Diskin, G. S., Dmitrovic,
 S., Edwards, E.-L., Fenn, M. A., Ferrare, R. A., van Gilst, D., Hair, J. W., Harper, D. B., Hilario, M. R. A., Hostetler, C. A., Jester, N.,
 Jones, M., Kirschler, S., Kleb, M. M., Kusterer, J. M., Leavor, S., Lee, J. W., Liu, H., McCauley, K., Moore, R. H., Nied, J., Notari, A.,
 Nowak, J. B., Painemal, D., Phillips, K. E., Robinson, C. E., Scarino, A. J., Schlosser, J. S., Seaman, S. T., Seethala, C., Shingler, T. J.,
 Shook, M. A., Sinclair, K. A., Smith Jr., W. L., Spangenberg, D. A., Stamnes, S. A., Thornhill, K. L., Voigt, C., Vömel, H., Wasilewski,
- A. P., Wang, H., Winstead, E. L., Zeider, K., Zeng, X., Zhang, B., Ziemba, L. D., and Zuidema, P.: Spatially coordinated airborne data and complementary products for aerosol, gas, cloud, and meteorological studies: the NASA ACTIVATE dataset, Earth System Science Data, 15, 3419–3472, https://doi.org/10.5194/essd-15-3419-2023, 2023.





- Sorooshian, A., Siu, L. W., Butler, K., Brunke, M. A., Cairns, B., Chellappan, S., Chen, J., Choi, Y., Crosbie, E. C., Cutler, L., DiGangi, J. P., Diskin, G. S., Ferrare, R. A., Hair, J. W., Hostetler, C. A., Kirschler, S., Kleb, M. M., Li, X.-Y., Liu, H., McComiskey, A., Namdari, S.,
 Painemal, D., Schlosser, J. S., Shingler, T., Shook, M. A., Silva, S., Sinclair, K., Smith, W. L., Soloff, C., Stamnes, S., Tang, S., Thornhill, K. L., Tornow, F., Tselioudis, G., Van Diedenhoven, B., Voigt, C., Vömel, H., Wang, H., Winstead, E. L., Xu, Y., Zeng, X., Zhang, B., Ziemba, L., and Zuidema, P.: The NASA ACTIVATE Mission, Bulletin of the American Meteorological Society, 106, E1517–E1538, https://doi.org/10.1175/BAMS-D-24-0136.1, 2025.
- Stevens, B., Cotton, W. R., Feingold, G., and Moeng, C.-H.: Large Eddy Simulations of Strongly Precipitating, Shallow, Stratocumulus-Topped Boundary Layers, J. Atmos. Sci, 55, 3616–3638, https://doi.org/10.1175/1520-0469(1998)055<3616:LESOSP>2.0.CO;2, 1998.
 - Suzuki, K., Nakajima, T. Y., and Stephens, G. L.: Particle Growth and Drop Collection Efficiency of Warm Clouds as Inferred from Joint CloudSat and MODIS Observations, Journal of the Atmospheric Sciences, 67, 3019–3032, https://doi.org/10.1175/2010jas3463.1, 2010.
 - Szczodrak, M., Austin, P. H., and Krummel, P. B.: Variability of Optical Depth and Effective Radius in Marine Stratocumulus Clouds, Journal of the Atmospheric Sciences, 58, 2912–2926, https://doi.org/10.1175/1520-0469(2001)058<2912:VOODAE>2.0.CO;2, 2001.
- Tang, S., Wang, H., Li, X.-Y., Chen, J., Sorooshian, A., Zeng, X., Crosbie, E., Thornhill, K. L., Ziemba, L. D., and Voigt, C.: Understanding aerosol–cloud interactions using a single-column model for a cold-air outbreak case during the ACTIVATE campaign, Atmospheric Chemistry and Physics, 24, 10 073–10 092, https://doi.org/10.5194/acp-24-10073-2024, 2024.
 - Tornow, F., Ackerman, A. S., and Fridlind, A. M.: Preconditioning of overcast-to-broken cloud transitions by riming in marine cold air outbreaks, Atmospheric Chemistry and Physics, 21, 12 049–12 067, https://doi.org/https://doi.org/10.5194/acp-21-12049-2021, 2021.
- Tornow, F., Ackerman, A. S., Fridlind, A. M., Tselioudis, G., Cairns, B., Painemal, D., and Elsaesser, G.: On the Impact of a Dry Intrusion Driving Cloud-Regime Transitions in a Midlatitude Cold-Air Outbreak, Journal of the Atmospheric Sciences, 80, 2881–2896, https://doi.org/10.1175/JAS-D-23-0040.1, 2023.
- Tornow, F., Fridlind, A., Tselioudis, G., Cairns, B., Ackerman, A., Chellappan, S., Painemal, D., Zuidema, P., Voigt, C., Kirschler, S., and Sorooshian, A.: Measurement report: A survey of meteorological and cloud properties during ACTIVATE's postfrontal flights and their suitability for Lagrangian case studies, Atmospheric Chemistry and Physics, 25, 5053–5074, https://doi.org/10.5194/acp-25-5053-2025, 2025.
 - Twomey, S.: Pollution and the planetary albedo, Atmospheric Environment, 8, 1251–1256, https://doi.org/10.1016/0004-6981(74)90004-3, 1974.
- Twomey, S.: The Influence of Pollution on the Shortwave Albedo of Clouds, J. Atmos. Sci., 34, 1149–1152, https://doi.org/10.1175/1520-0469(1977)034<1149:TIOPOT>2.0.CO;2, 1977.
 - vanZanten, M. C., Stevens, B., Vali, G., and Lenschow, D. H.: Observations of Drizzle in Nocturnal Marine Stratocumulus, J. Atmos. Sci, 62, 88–106, https://doi.org/10.1175/JAS-3355.1, 2005.
 - Wang, H. and Feingold, G.: Modeling Mesoscale Cellular Structures and Drizzle in Marine Stratocumulus Part I: Impact of Drizzle on the Formation and Evolution of Open Cells, J. Atmos. Sci, 66, 3237–3256, https://doi.org/10.1175/2009JAS3022.1, 2009.
- Wang, S., Wang, Q., and Feingold, G.: Turbulence, Condensation, and Liquid Water Transport in Numerically Simulated Nonprecipitating Stratocumulus Clouds, J. Atmos. Sci, 60, 262–278, https://doi.org/10.1175/1520-0469(2003)060<0262:TCALWT>2.0.CO;2, 2003.
 - Wegener, A.: Thermodynamik der Atmosphäre, Nature, 90, https://doi.org/10.1038/090031a0, 1912.
 - Wood, R.: Stratocumulus Clouds, Mon. Wea. Rev., 140, 2373-2423, https://doi.org/10.1175/MWR-D-11-00121.1, 2012.
- Wu, P. and Ovchinnikov, M.: Cloud Morphology Evolution in Arctic Cold-Air Outbreak: Two Cases During COMBLE Period, Journal of Geophysical Research: Atmospheres, 127, https://doi.org/10.1029/2021JD035966, 2022.





- Wyant, M. C., Bretherton, C. S., Rand, H. A., and Stevens, D. E.: Numerical Simulations and a Conceptual Model of the Stratocumulus to Trade Cumulus Transition, J. Atmos. Sci., 54, 168–192, https://doi.org/10.1175/1520-0469(1997)054<0168:NSAACM>2.0.CO;2, 1997.
- Xue, H. and Feingold, G.: Large-Eddy Simulations of Trade Wind Cumuli: Investigation of Aerosol Indirect Effects, J. Atmos. Sci, 63, 1605–1622, https://doi.org/10.1175/JAS3706.1, 2006.
- 420 Yamaguchi, T., Feingold, G., and Kazil, J.: Stratocumulus to Cumulus Transition by Drizzle, J. Adv. Model. Earth Syst., 9, 2333–2349, https://doi.org/10.1002/2017MS001104, 2017.
 - Zelinka, M. D., Myers, T. A., McCoy, D. T., Po-Chedley, S., Caldwell, P. M., Ceppi, P., Klein, S. A., and Taylor, K. E.: Causes of Higher Climate Sensitivity in CMIP6 Models, Geophysical Research Letters, 47, https://doi.org/https://doi.org/10.1029/2019GL085782, 2020.
 - Zhang, J. and Feingold, G.: Distinct regional meteorological influences on low-cloud albedo susceptibility over global marine stratocumulus regions, Atmos. Chem. Phys., 23, 1073–1090, https://doi.org/10.5194/acp-23-1073-2023, 2023.
 - Zhang, J., Zhou, X., Goren, T., and Feingold, G.: Albedo susceptibility of northeastern Pacific stratocumulus: the role of covarying meteorological conditions, Atmos. Chem. Phys., 22, 861–880, https://doi.org/10.5194/acp-22-861-2022, 2022.
- Zhang, J., Chen, Y.-S., Yamaguchi, T., and Feingold, G.: Cloud water adjustments to aerosol perturbations are buffered by solar heating in non-precipitating marine stratocumuli, Atmospheric Chemistry and Physics, 24, 10425–10440, https://doi.org/10.5194/acp-24-10425-2024, 2024.





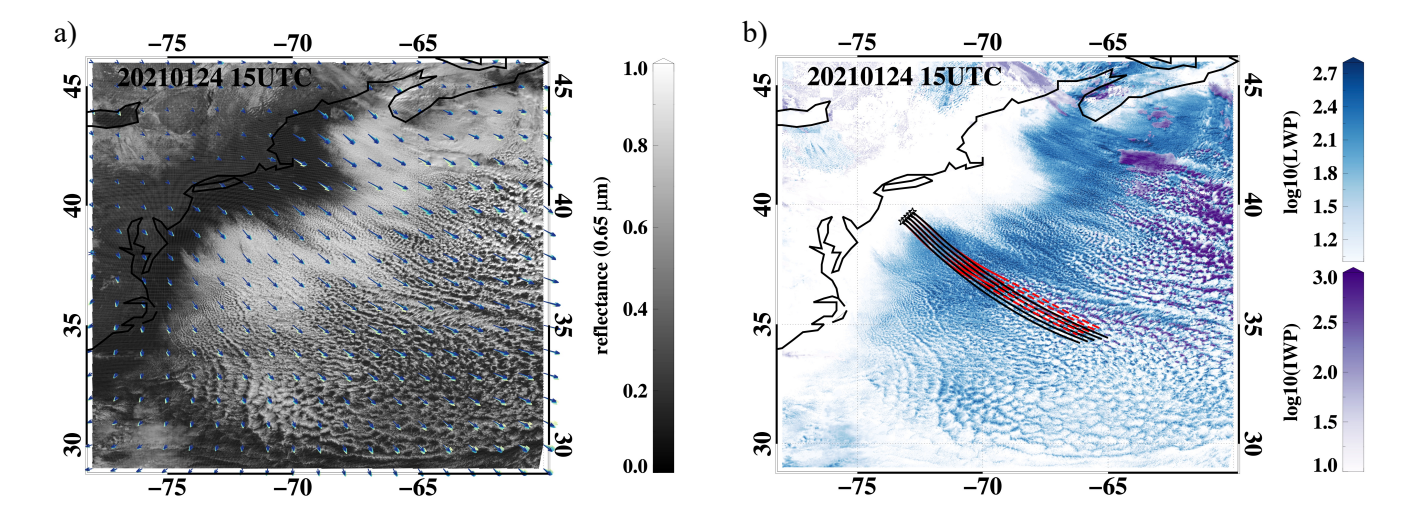


Figure 1. GOES-16 images and SatCORPS retrievals of the MCAO event at 15 UTC on January 24, 2021. (a) Reflectance at 0.65 μm, overlaid with 1000 hPa wind vectors from ERA5 (7–15 UTC, from warm to cold colors). (b) Common logarithm of cloud liquid water path (LWP; shades of blue) and ice water path (IWP; shades of purple), overlaid with five 1000-hPa-wind-advected isobaric, forward Lagrangian trajectories starting from western cloud edge at 13 UTC for 15 hours (locations indicated by the black open stars), with solid red indicating trajectories during sunlit hours (13–21 UTC) and dashed red indicating the remaining nighttime hours. Instantaneous trajectories, based on the wind field at 15 UTC for 15 hours, are indicated in black solid lines.

Table 1. Selected MCAO events during ACTIVATE (2020–2022), including date, initial location (central of the five) and duration of the instantaneous trajectories.

Date	Longitude (°)	Latitude (°)	Duration (hr)
2020-03-01	-73.5	39.5	12
2021-01-29	-75.5	36.5	12
2022-01-11	-73.8	39.5	12
2022-01-18	-73.5	38.5	12
2022-03-29	-73.8	38.8	12





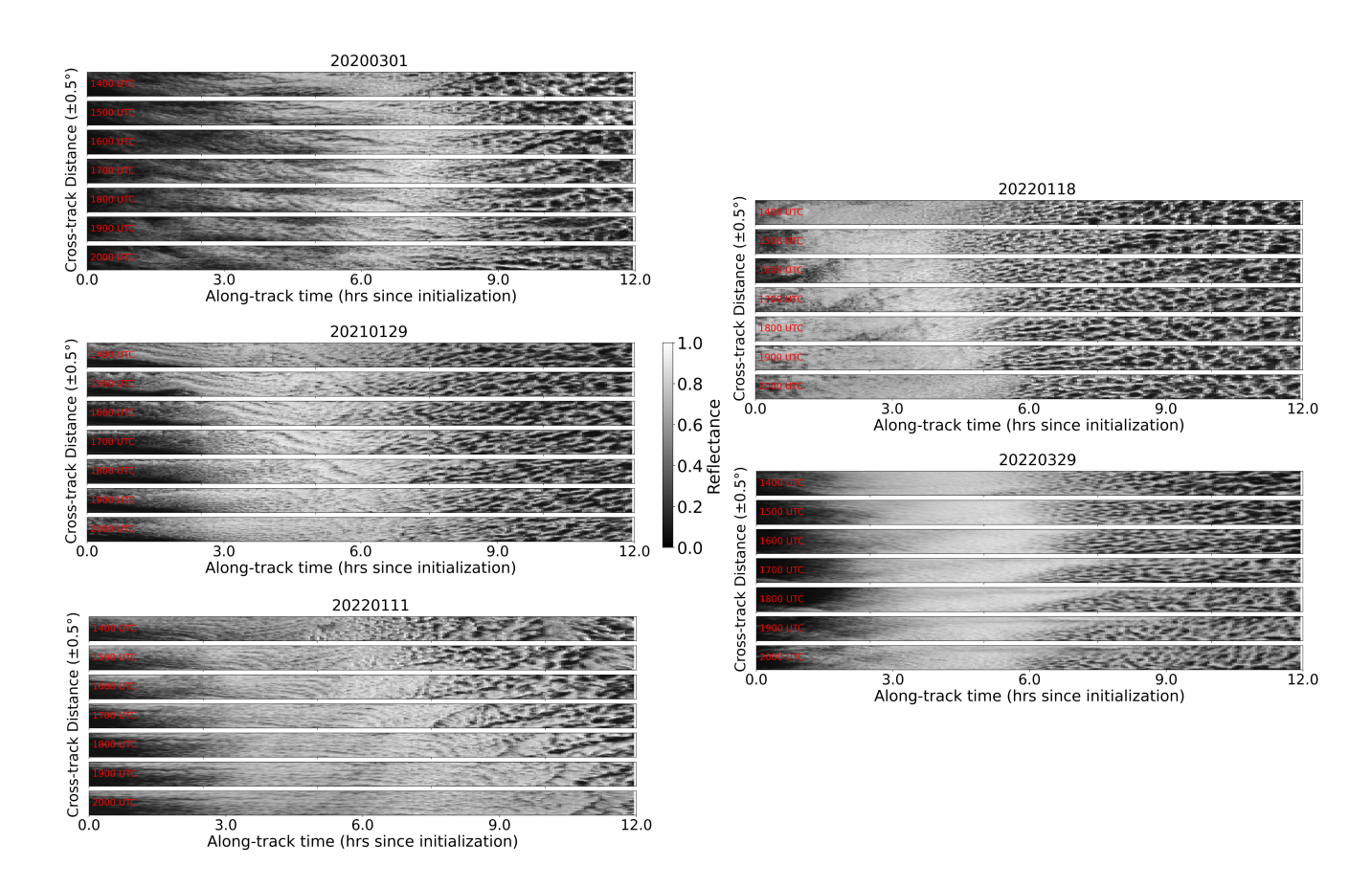


Figure 2. GOES-16 images of $0.65 \mu m$ reflectance oriented along 12-hr instantaneous trajectories during sunlit hours from 14 to 20 UTC, for the five MCAO events.





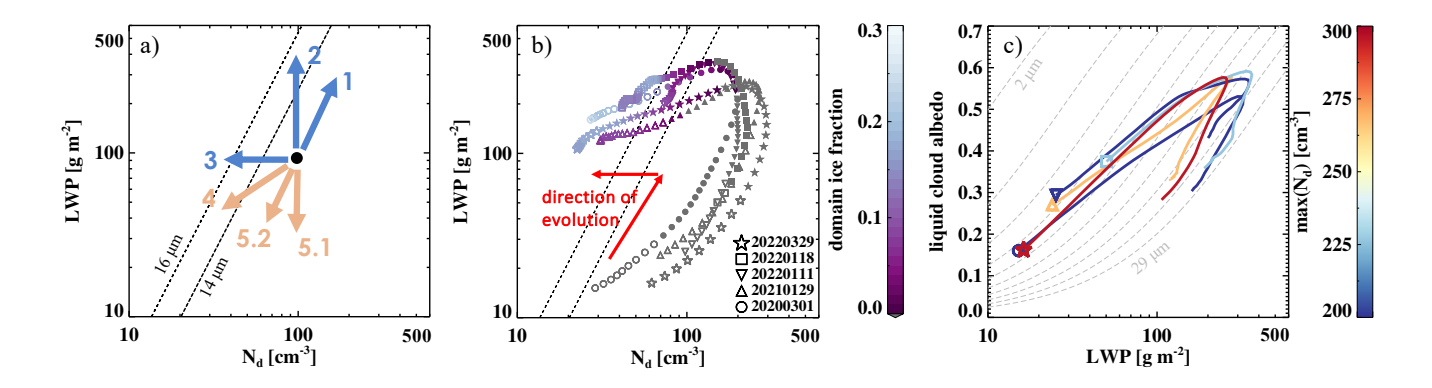


Figure 3. Cloud evolution along instantaneous trajectories during MCAO, based on GOES-16 SatCORPS retrievals. (a) A diagram identifying how individual processes drive the system in LWP- N_d space (1. activation-growth, 2. condensational-growth, 3. collision-coalescence, 4. precipitation, 5. entrainment (5.1: homogeneous, 5.2: inhomogeneous). Isolines of r_e of 14 and 16 μm based on an adiabatic condensation rate of 2.16·10⁶ kg m⁻⁴ are indicated in black dashed lines. (b) Mean traces, averaged across 14-20 UTC, through the scene in LWP- N_d space. Each MCAO event is label with different symbols, with open (filled) symbols indicating broken (overcast) conditions. Fraction of ice-phase pixels within the 1° by 1° domain is indicated by color, with gray color indicating a liquid-only scene. (c) Mean traces through the scene in SatCORPS-retrieved liquid cloud albedo - LWP space. Color of the traces indicate the maximum N_d of the event. Symbol represents event date with its location indicating the start of the trajectory. Gray, dashed isolines indicate constant r_e values, ranging from 2 to 29 μm (increment of 3) based on 2-stream approximation.





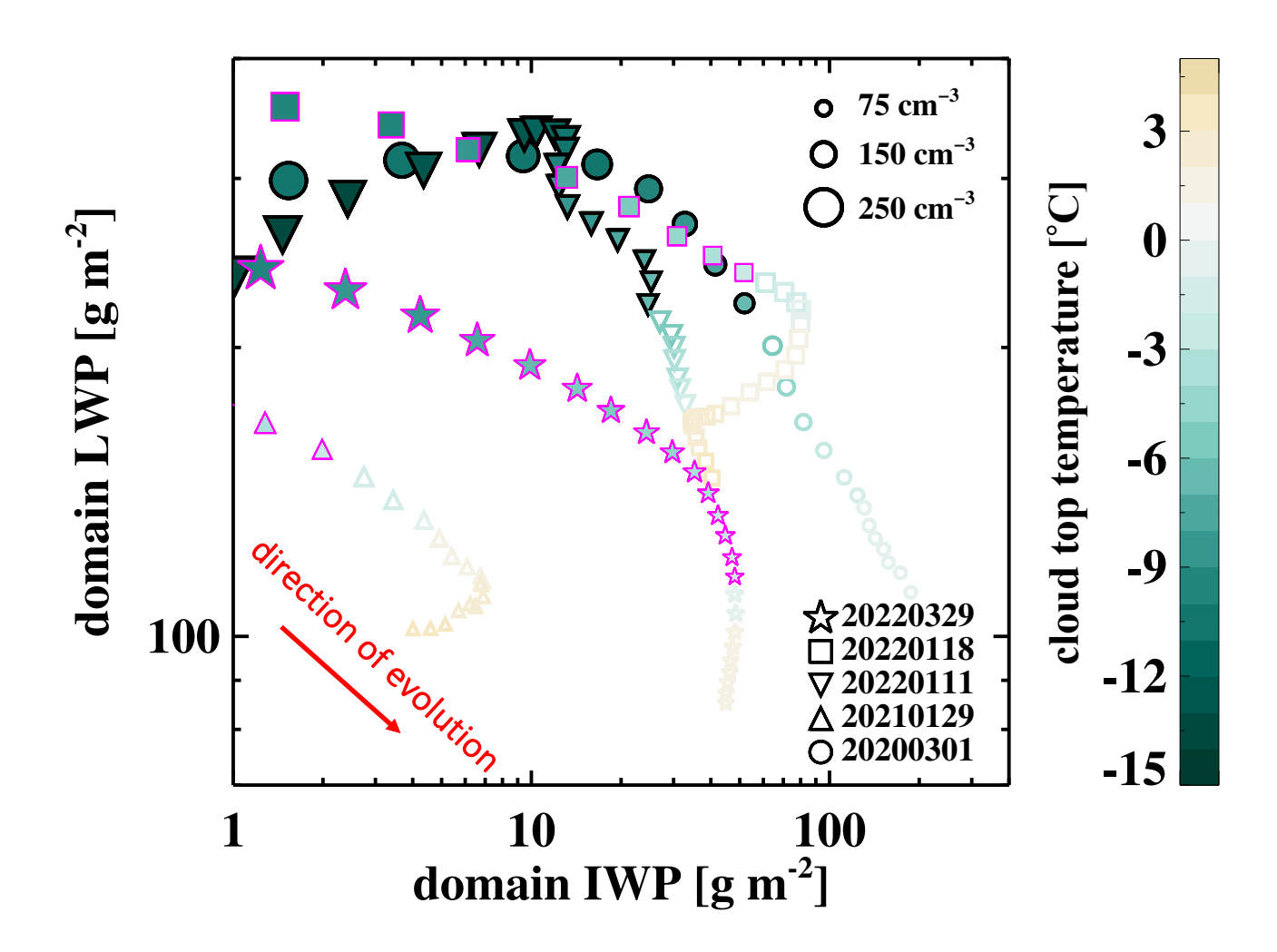


Figure 4. Traces of cloud evolution since ice formation along instantaneous trajectories through MCAO scenes in domain-LWP-vs-domain-IWP space. Colors indicate cloud top temperatures. Symbols represent event dates, with open (filled) symbols indicating broken (overcast) conditions and their sizes indicating $N_{\rm d}$.





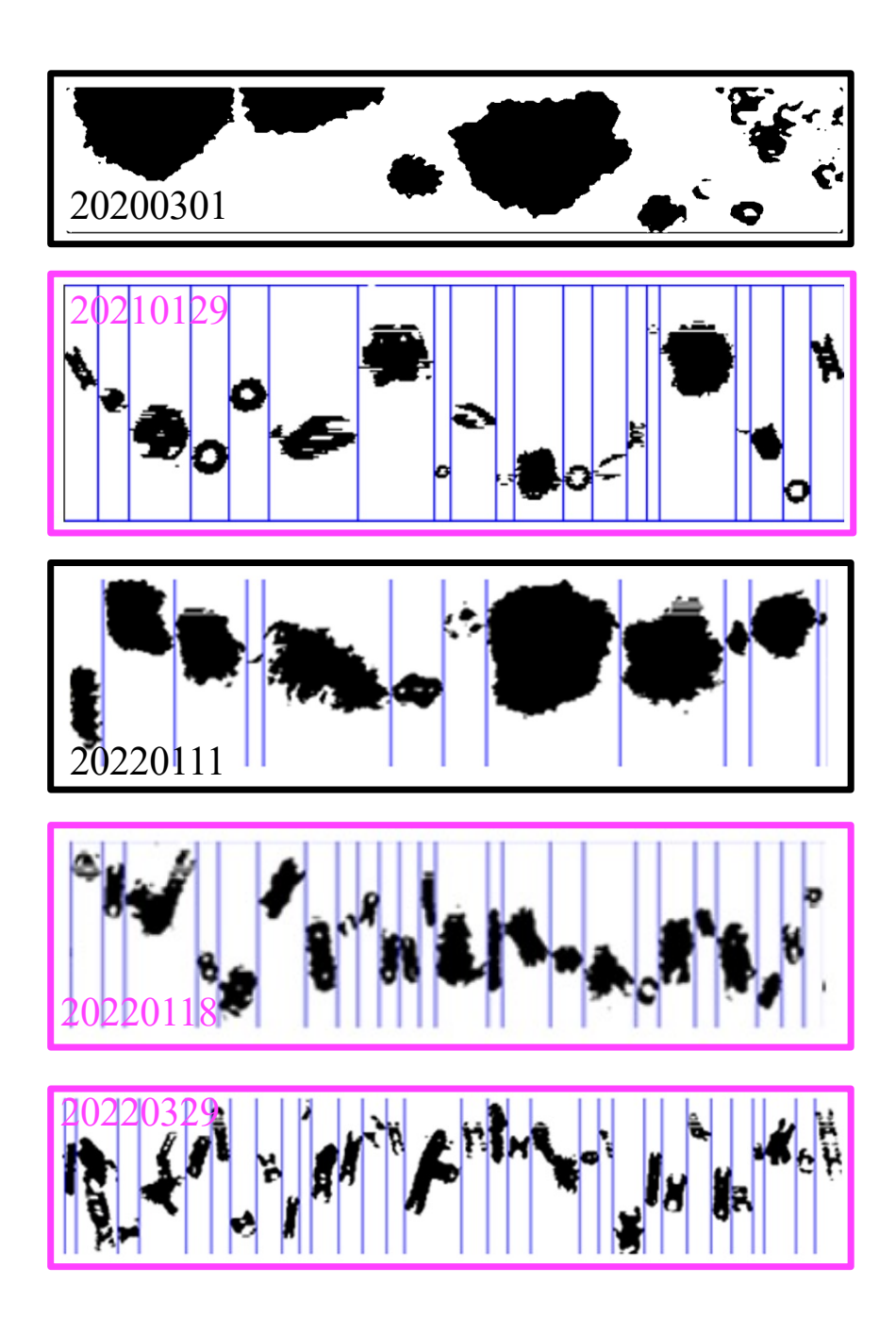


Figure 5. Exemplary 2DS ice habit images taken close to the onset of cloud transition during the above-cloud-base (ACB) leg for each MCAO event. Dates are color-coded as in the colors of the symbol outlines in Figure 4.





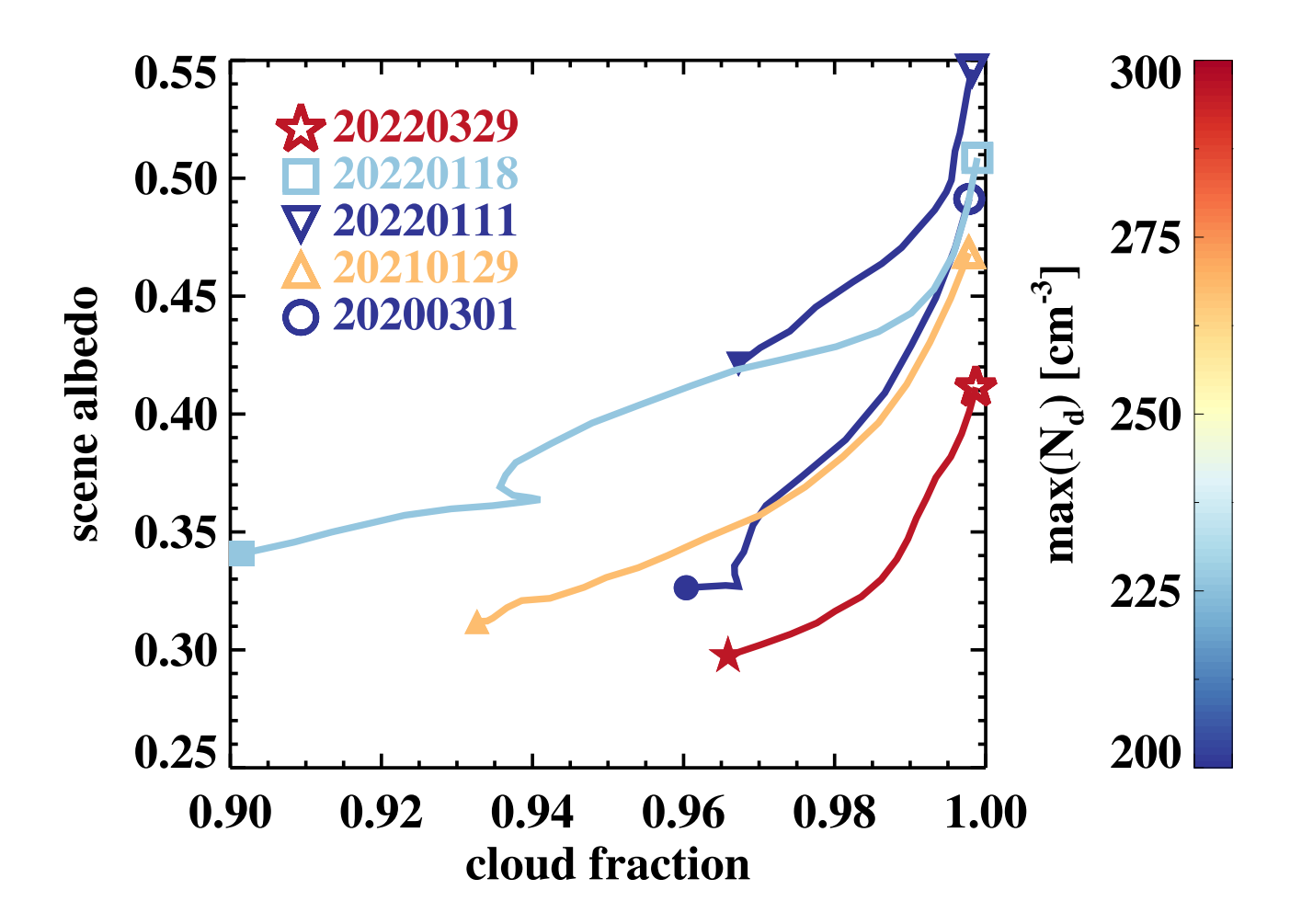


Figure 6. Traces of cloud evolution since cloud breakup along instantaneous trajectories through MCAO scenes in SatCORPS-retrieved scene albedo versus cloud fraction. Color of the trace denotes the maximum N_d of the event. Open and filled symbols represent event date with their locations denoting cloud breakup and the end of trajectory, respectively.





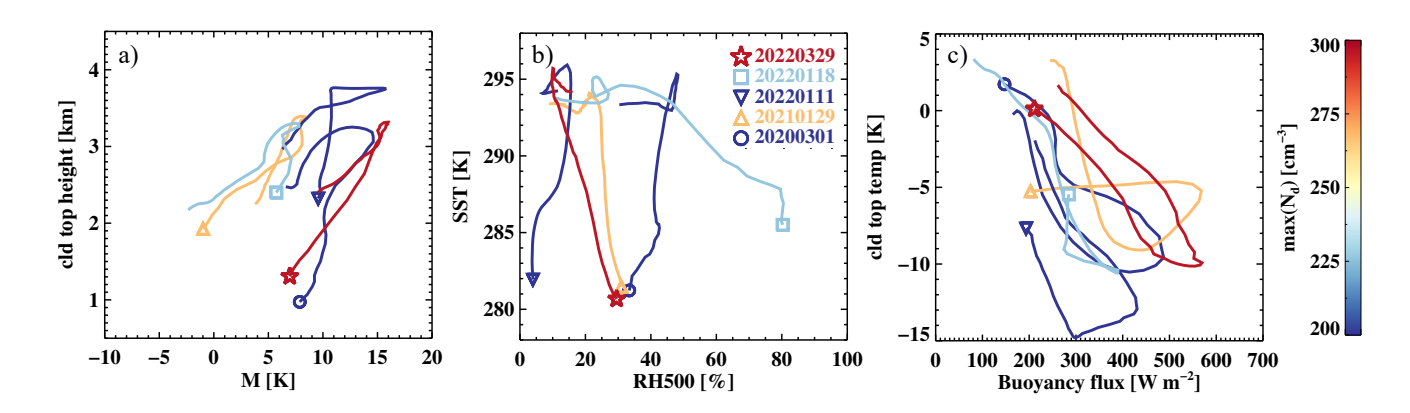


Figure 7. Traces of boundary layer evolution along instantaneous trajectories through MCAO scenes in **a**) cloud top height versus M-index space, **b**) SST-RH_{500mb} space, and **c**) cloud top temperature versus buoyancy flux space. Colors indicate cloud top temperatures. Symbol represents event date with its location indicating the start of the trajectory.





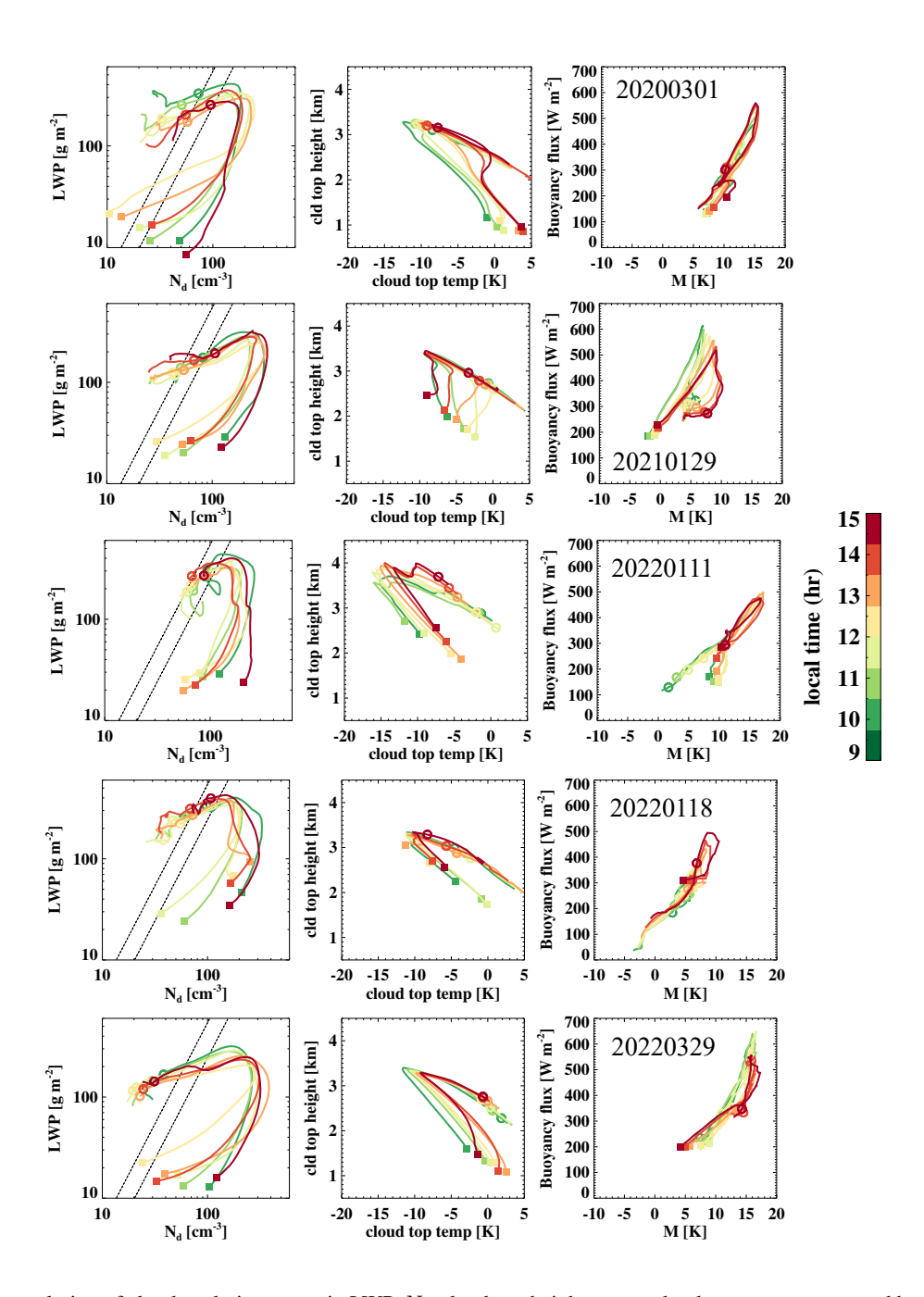


Figure 8. Daytime evolution of cloud evolution traces in LWP- N_d , cloud-top height versus cloud-top temperature, and buoyancy flux versus M-index spaces for the five MCAO events. Color of the trace denotes local time from 9 to 15, and the beginning of the trace is indicated by filled squares, with open circles representing the onset of cloud breakup (overcast-to-broken transition).





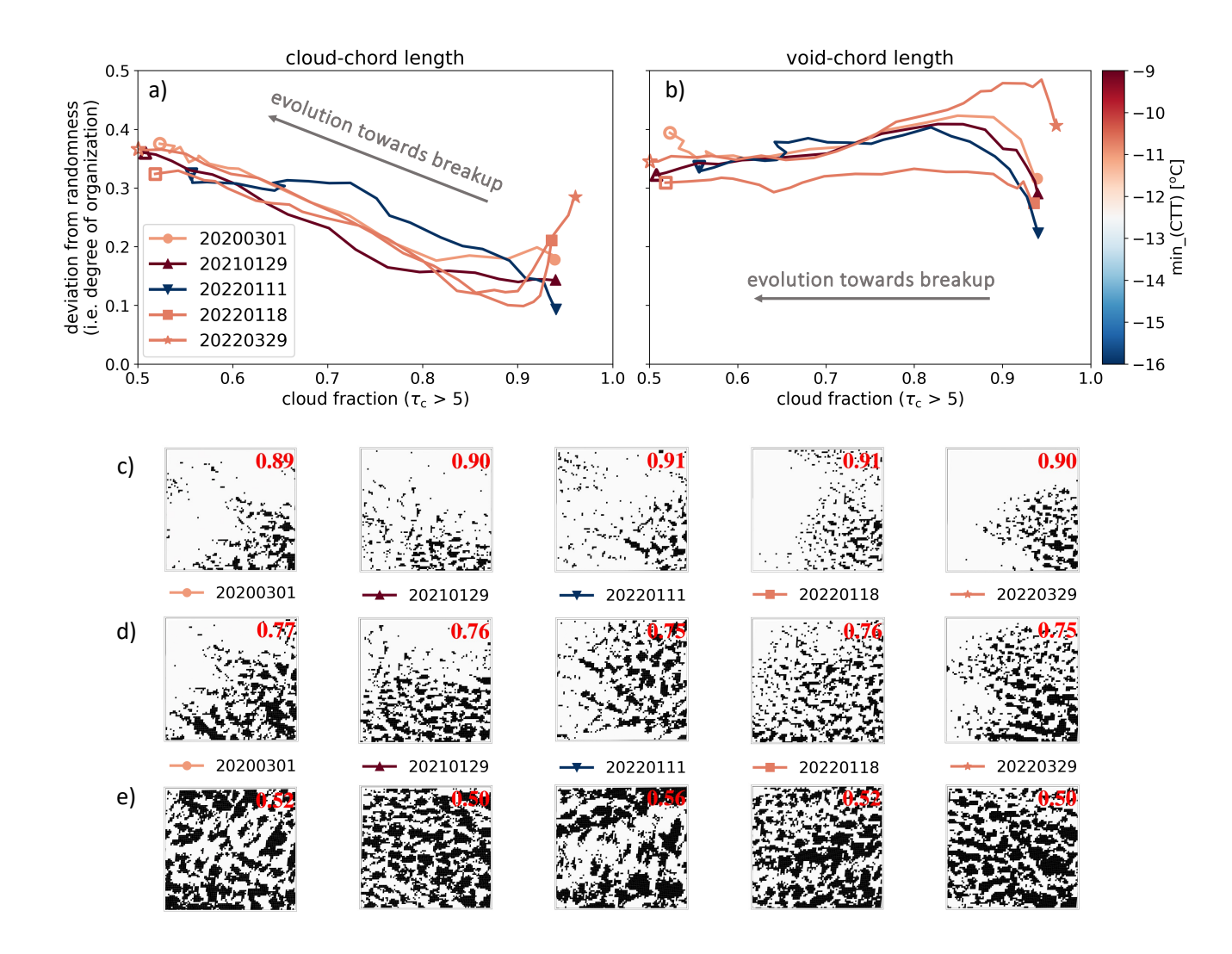


Figure 9. Metrics of cloud organization as a function of cloud fraction during cloud transition from overcast to broken fields for the five MCAO events at 15 UTC. Color of the trace denotes the minimum cloud top temperature reached, with beginning (end) of the trace indicated by filled (open) symbols. Degree of organization is expressed in the form of deviation from randomness for (a) cloud-chord length and (b) void-chord length, following Koren et al. (2024). 2° by 2° binary cloud mask fields at cloud fraction of (c) \sim 0.9, (d) \sim 0.75, and (e) the end of each transition, with white areas indicating cloudy pixels, defined as GOES-16 retrieved cloud optical depth (τ_c) > 5. Cloud fraction is noted in red on each snapshot.